UNIVERSITY OF HELSINKI

https://helda.helsinki.fi

# Classifying the Magnetosheath Using Local Measurements From MMS

**Svenningsson, Ida; Yordanova, Emiliya; Khotyaintsev, Y. V.; André, M.; Cozzani, Giulia**

**2025-01**
Wiley Blackwell
http://hdl.handle.net/10138/593382
Svenningsson, I, Yordanova, E, Khotyaintsev, Y V, André, M & Cozzani, G 2025, 'Classifying the Magnetosheath Using Local Measurements From MMS', Journal of geophysical research. Space physics, vol. 130, no. 1, e2024JA033272. https://doi.org/10.1029/2024ja033272

Downloaded from Helda, University of Helsinki institutional repository. https://helda.helsinki.fi
This is an electronic reprint of the original article.
This reprint may differ from the original in pagination and typographic detail.
Please cite the original version.

Check for updates

JGR Space Physics

RESEARCH ARTICLE
10.1029/2024JA033272

# Classifying the Magnetosheath Using Local Measurements From MMS

I. Svenningsson[1,2], E. Yordanova[1], Y. V. Khotyaintsev[1,2], M. André[1], and G. Cozzani[3]

[1]Swedish Institute of Space Physics, Uppsala, Sweden, [2]Department of Physics and Astronomy, Uppsala University, Uppsala, Sweden, [3]Department of Physics, University of Helsinki, Helsinki, Finland

**Key Points:**

- We present a method for classifying the magnetosheath using local MMS measurements
- Local magnetic field fluctuations and ion temperature anisotropy are used to classify the magnetosheath in two configurations
- MMS burst-mode data is required to quantify suprathermal ions due to on-board compression of fast-mode data

**Supporting Information:**

Supporting Information may be found in the online version of this article.

**Correspondence to:**

I. Svenningsson,
ida.svenningsson@irf.se

**Citation:**

Svenningsson, I., Yordanova, E., Khotyaintsev, Y. V., André, M., & Cozzani, G. (2025). Classifying the magnetosheath using local measurements from MMS. *Journal of Geophysical Research: Space Physics*, *130*, e2024JA033272. https://doi.org/10.1029/2024JA033272

Received 4 SEP 2024
Accepted 5 DEC 2024

©2024. The Author(s).
This is an open access article under the terms of the Creative Commons Attribution License, which permits use, distribution and reproduction in any medium, provided the original work is properly cited.

**Abstract** The Earth's magnetosheath is a dynamic region of shocked solar wind plasma downstream of the bow shock. Depending on the upstream magnetic field orientation, the magnetosheath usually has one of two distinct configurations: a more variable magnetosheath with strong fluctuations and structures propagating from upstream to downstream, or a more stationary magnetosheath characterized by compression and high ion temperature anisotropy. The more variable magnetosheath is usually observed for quasi-parallel shocks (the angle between the shock normal and the upstream magnetic field $\theta_{Bn} < 45°$), but the limit can vary for $40° \leq \theta_{Bn} \leq 70°$. These differences facilitate studies of how different plasma environments affect various processes such as turbulence and heating, and these require an accurate magnetosheath classification. Since $\theta_{Bn}$ can rarely be determined correctly in the absence of upstream monitors, local measurements have been suggested to classify the magnetosheath. However, this has not yet been verified for Magnetospheric Multiscale (MMS) data. We investigate this approach with MMS using locally measured magnetic field variability, ion temperature anisotropy, and suprathermal ion flux. We find the more variable magnetosheath at normalized magnetic fluctuations above 0.29 and ion temperature anisotropy below 0.18. We also find that the suprathermal ion flux can complement the classification given that MMS burst-mode data is used. Our findings provide a method to determine the magnetic connectivity of the magnetosheath with the upstream solar wind in the case of MMS and classify the downstream region into different configurations.

## 1. Introduction

The Earth's magnetosheath (MSH) consists of compressed and heated solar wind which has interacted with the bow shock (BS) and is deflected around the magnetosphere. The plasma conditions in the MSH can be divided into two main categories. These are in many cases well separated by the shock normal angle $\theta_{Bn}$, that is, the angle between the upstream interplanetary magnetic field (IMF) and the normal direction of the shock surface: $\theta_{Bn} < 45°$ is considered quasi-parallel $\left(Q_{\parallel}\right)$ and $\theta_{Bn} > 45°$ quasi-perpendicular ($Q_{\perp}$). The two geometries determine distinct plasma conditions, which in turn lead to different plasma processes. As a result, it is helpful to have reliable methods to classify data samples in the respective MSH configurations.

The $Q_{\parallel}$ MSH typically has a more fluctuating nature than the $Q_{\perp}$ MSH, for example, in small-scale ion flux (Shevyrev et al., 2007), and both transverse and compressional fluctuations in the magnetic field (Dimmock et al., 2014; Luhmann et al., 1986) and velocity (Dimmock et al., 2015). One of the main factors for this variability is the ion foreshock, which forms when $\theta_{Bn}$ is small, and ions reflected by the shock excite fluctuations in the upstream plasma. The reflected ion population, also referred to as the field-aligned ion beam (FAB), connects to the BS at $\theta_{Bn} > 30°$ (Paschmann et al., 1981). The reflected ion distributions evolve with distance from the foreshock edge (Kempf et al., 2015). Further in, the foreshock contains a diffuse ion population that is associated with ultralow frequency (ULF) waves, located in the so-called ULF foreshock with an upper boundary observed for $\theta_{Bn} \in (35°, 65°)$ (Le & Russell, 1992). Turc et al. (2023) used simulations and spacecraft observations to show a direct link between the foreshock waves and MSH fluctuations, suggesting that they pass through the shock into the MSH. The $Q_{\parallel}$ MSH is also characterized by a population of high-energy ions (Asbridge et al., 1978) originating from the BS (Burgess et al., 2012; Fuselier et al., 1991). Such ions with energy above 3 keV have been observed in the MSH downstream of shocks with $\theta_{Bn} < 60°$ (Crooker et al., 1981). It has been observed in-situ and in simulations (Johlander et al., 2021; Lalti et al., 2022) that the $Q_{\parallel}$ BS can accelerate ions to energies larger than 10 times the solar wind bulk energy, creating a suprathermal tail in the downstream ion distribution. Without the upstream connection, typically at $Q_{\perp}$ shocks, reflected ions remain in the vicinity of the

21699402, 2025, 1, Downloaded from https://agupubs.onlinelibrary.wiley.com/doi/10.1029/2024JA033272 by University Of Helsinki, Wiley Online Library on [03/03/2025]. See the Terms and Conditions (https://onlinelibrary.wiley.com/terms-and-conditions) on Wiley Online Library for rules of use; OA articles are governed by the applicable Creative Commons License

shock where the convection electric field accelerates them perpendicularly to the upstream magnetic field (Treumann, 2009). This, combined with adiabatic compression of ions transmitted through the shock, results in a high temperature anisotropy $T_{i\perp}/T_{i\parallel} > 1$ in the $Q_\perp$ MSH, where $T_{i\perp}$ and $T_{i\parallel}$ are the temperatures perpendicular and parallel to the background magnetic field, respectively (Dimmock et al., 2015).

The MSH has been studied extensively for decades (Narita et al., 2021, and references therein). However, fewer studies focus on comparing the different processes favored by the local conditions in the $Q_\parallel$ and $Q_\perp$ MSH configurations. For example, ion cyclotron (Alexandrova et al., 2008), mirror-mode (Dimmock et al., 2015; Soucek et al., 2015) and whistler (Svenningsson et al., 2024) waves are found to be more common in the $Q_\perp$ MSH. In the $Q_\parallel$ MSH, structures such as current sheets (Chasapis et al., 2015; Vörös et al., 2016; Yordanova et al., 2020) and MSH jets (Hietala et al., 2009; Plaschke et al., 2013; Raptis et al., 2020) are more common. So, the $Q_\parallel$ MSH hosts the physical processes related to these structures, such as magnetic reconnection (Phan et al., 2018; Retinò et al., 2007; Stawarz et al., 2019; Vörös et al., 2017; Yordanova et al., 2016), particle acceleration (E. Eriksson et al., 2016; Jarvinen et al., 2018; Retinò et al., 2007) and plasma heating (Breuillard et al., 2018; Chasapis et al., 2015, 2018; S. Eriksson et al., 2016; Yordanova et al., 2021). Other comparisons between the MSH geometries have included spectral characteristics of the electromagnetic fields (Breuillard et al., 2018; Czaykowska et al., 2001; Yordanova et al., 2020) and the ion flux (Rakhmanova et al., 2018). Among the many spacecraft studying the MSH, the Magnetospheric Multiscale (MMS) (Burch et al., 2016) is the multi-spacecraft mission with the closest spacecraft separation and highest temporal resolution, specialized to resolve electron-scale phenomena. The need for a deeper understanding of the MSH has motivated the MMS community to implement the *unbiased MSH campaign*. This campaign is aimed at collecting a large set of high-resolution measurements along MSH crossings to allow for statistical investigations.

The MSH is a very well-suited region for detailed studies of various plasma processes due to two key reasons. The first is the availability of multi-point measurements from spacecraft missions, such as THEMIS, Cluster, and MMS. Studies based on these missions have shown the statistical dependence of the MSH from the variable upstream solar wind conditions (Ma et al., 2024; Michotte De Welle et al., 2024, and references therein), resulting in a broad plasma parameters' space accessible in the MSH (Dimmock et al., 2017; Gutynska et al., 2008, and references therein). Multi-point techniques in such a broad parameter space allow the inherent 3D nature of the plasma fluctuations to be assessed, and for example, different wave vectors (Narita et al., 2006) and spatial gradients (Dunlop et al., 2021; Yordanova et al., 2021, and references therein) to be estimated. Furthermore, in the MSH, the typical plasma density is relatively high compared to other space plasma regions. This higher density mitigates challenges associated with lower particle counts, making it easier to accurately estimate plasma moments (Roberts et al., 2023). Comparative studies of small-scale physical processes in the $Q_\parallel$ and $Q_\perp$ MSH, however, come mostly from case studies or small data sets, and statistics are needed to verify whether the observed phenomena are typical for a certain MSH configuration. This requires an accurate classification which is challenging to do for longer periods of time, considering the continuously changing solar wind conditions and the lack of upstream monitors in the immediate vicinity of the BS. For MSH statistical studies, it is crucial to keep in mind the potential biases introduced in the data sets by the specific orbit (e.g., polar or equatorial) of the different spacecraft missions, crossing the MSH at different locations, different spacecraft formations (tetrahedron vs. string-of-pearls) and inter-spacecraft (MHD- vs. ion- vs. electron-scales) separations, and characteristics (sampling rate, calibration, and telemetry) in spacecraft instrumentation. While considering these challenges, it is necessary to develop methods to robustly classify the magnetosheath observations and distinguish the $Q_\parallel$ MSH from the $Q_\perp$ MSH.

One way to classify the MSH is by calculating $\theta_{Bn}$, for example, by using a model BS (e.g., Farris et al., 1991; Merka et al., 2003, and references therein) and upstream magnetic field measured by spacecraft orbiting the 1$^{st}$ Lagrangian point (L1). This method relies on the availability of L1 measurements. Also, measurements at L1 do not always accurately describe the solar wind hitting the BS due to variation in the solar wind flow and spacecraft offset relative to the Sun-Earth line (Borovsky, 2018; Di Matteo & Sivadas, 2022). The upstream magnetic field direction can also be measured directly at the shock, as in for example, Karlsson et al. (2021). This, however, can only be done close to a shock crossing, and the MSH geometry could change as the spacecraft moves further downstream. Other studies combine BS models with MSH flow models to connect a plasma parcel inside the MSH with its origin at the BS (Génot et al., 2011; Soucek & Escoubet, 2012; Turc et al., 2014). This approach assumes that the BS position stays the same during the propagation from the BS to the spacecraft location. Thus,

21699402, 2025, 1, Downloaded from https://agupubs.onlinelibrary.wiley.com/doi/10.1029/2024JA033272 by University Of Helsinki, Wiley Online Library on [03/03/2025]. See the Terms and Conditions (https://onlinelibrary.wiley.com/terms-and-conditions) on Wiley Online Library for rules of use; OA articles are governed by the applicable Creative Commons License

while these methods improve the classification, the exact value of $\theta_{Bn}$ relevant to a given set of MSH measurements is rarely possible to determine, even for multi-spacecraft missions. In many cases, we rely on the ability to determine whether the MSH is downstream of the ion foreshock or not. Moreover, since the ion foreshock boundary can be found at different values of $\theta_{Bn}$ depending on the upstream conditions, the shock geometry does not fully describe the physical conditions in the MSH. Hence, complementary approaches are essential for categorizing the MSH.

In the last years, there has been increasing interest in using local MSH parameters to distinguish between the MSH configurations (Karlsson et al., 2021; Koller et al., 2024; Raptis et al., 2020). This approach has been verified by Karlsson et al. (2021) with data from the Cluster mission (Escoubet et al., 1997) using a total of 3.6 hr of data from nine orbits during 2003–2009. Having one spacecraft upstream of the BS and one downstream in the MSH, they could directly measure $\theta_{Bn}$ and relate it to the downstream magnetic field standard deviation, ion temperature anisotropy, and ion flux above 10 keV. Their results showed that a combination of these parameters provides a good set of indicators to classify a given MSH interval as having the properties typical of either the $Q_{\parallel}$ or $Q_{\perp}$ MSH without knowledge of the upstream conditions. They also observed a transition region between $\theta_{Bn}$ values of approximately 45° and 60° in which the MSH could display traits typical for both geometries, which may be attributed to the moving foreshock boundary. This approach is promising and should be further verified using larger data sets and a variety of plasma conditions and spacecraft locations.

Among the indicators used for the MSH classification, the detection of energetic ions is particularly delicate as it depends on the noise level of the particle instrument used (Karlsson et al., 2021). Therefore, before making use of this method on MMS data, instrument peculiarities should be properly investigated. In addition, the present quantification of energetic ions is not viable for varying upstream conditions. Using the THEMIS mission (Angelopoulos, 2008) and the method proposed by Karlsson et al. (2021), Koller et al. (2024) found a significantly higher flux of high-energy ions (>8 keV) in the MSH in cases with fast (coronal-hole originated) solar wind upstream of the shock. This complicates the MSH classification and calls for further investigation of the quantification of energetic ions before applying the method to MMS data.

In this study, we investigate the use of local plasma parameters to separate the two MSH configurations by adopting an approach similar to Karlsson et al. (2021) and applying it to the MMS mission. In Section 2 we describe our data set, the magnetosheath geometry estimation and define the local parameters. We also describe important considerations to be made when quantifying suprathermal ions, instrumental (specific to MMS) as well as physical. In Section 3 we compare the local parameters to the magnetosheath geometry and assess how well the local parameters distinguish between the two MSH configurations. Finally, we discuss the results in Section 4 and give conclusions in Section 5.

## 2. Methods

We use measurements from the MMS mission (Burch et al., 2016). The magnetic field vector $\boldsymbol{B}$ is measured with 128 samples/s by the flux-gate magnetometer (FGM) (Russell et al., 2016). The fast plasma investigation (FPI) (Pollock et al., 2016) instruments provide 3D ion velocity distributions and the derived moments, with a time resolution of 150 ms in burst mode and 4.5 s in fast mode. Fast-mode data is always available in the MSH, while the highest-resolution burst-mode measurements have lower availability due to telemetry limitations. In this study, we mainly use burst-mode data. On MMS, burst-mode intervals are chosen manually by a scientist in the loop (Fuselier et al., 2016), which naturally leads to a bias toward unusual or interesting structures such as current sheets, jets, reconnection sites, or sharp boundaries. Here, we want to avoid this selection bias to get an idea of the normal background MSH conditions. Therefore, we use data from the *unbiased MSH campaign* from February to March 2023. During this campaign, 3-min intervals of burst-mode data were downlinked every 9 min for 14 MSH crossings. Since this campaign mainly contained $Q_{\perp}$ MSH, we complement the data set with intervals from 2018 to 2020 chosen to study MSH turbulence without targeting specific structures. This data set gives a good coverage of shock geometries (see the calculation of $\theta_{Bn}$ below) and MSH conditions. While the lower-resolution, fast-mode data has higher availability, we use only the intervals for which there are high-resolution burst-mode measurements, necessary to correctly identify the energetic ion flux (as described in Section 2.2.1). In total, we have 47 MSH crossings measured by MMS1 during 2018–2023 adding up to 27.4 hr of burst measurements subdivided into 3,292 30-s intervals. Details about these intervals can be found in Table S1. We show the spatial

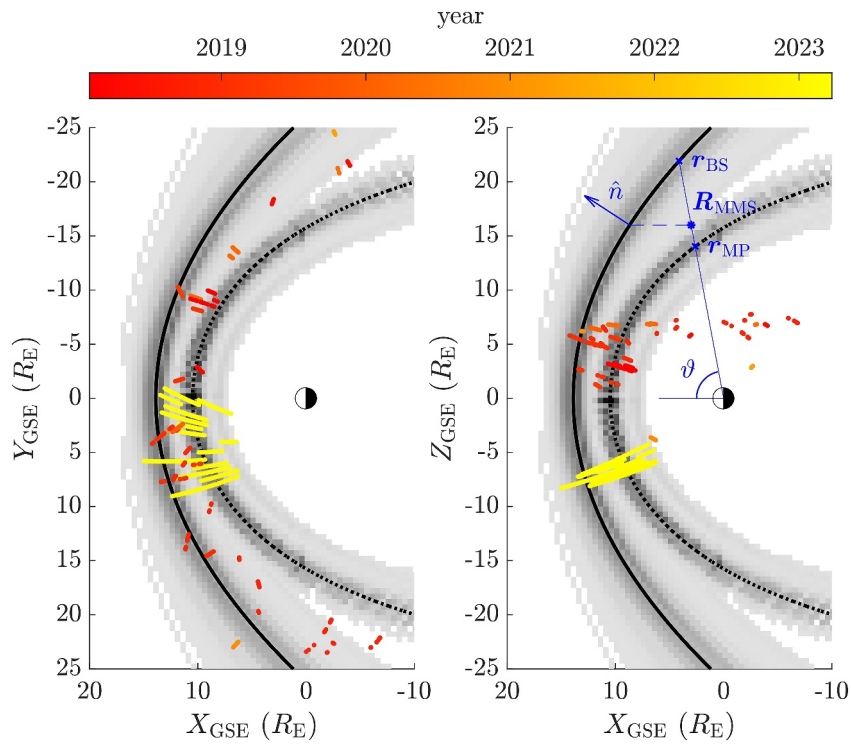



**Figure 1.** MMS locations for the burst data intervals used in this study. The color shows the time of measurement with the 2023 unbiased MSH campaign in yellow. The bow shock (BS) (solid) and MP (dotted) are drawn for average solar wind parameters, and the grayscale shows the variations of the BS and MP in our data set. We also illustrate the estimation of the shock normal $\hat{n}$ and $\boldsymbol{r}_{MP}$ and $\boldsymbol{r}_{BS}$ used to calculate $d_{MP-BS}$ in Equation 3. The example is drawn in the $(X_{GSE}, Z_{GSE})$ plane assuming $Y_{GSE} = 0$ for illustration purposes.

distribution of our MSH intervals in Figure 1, color coded by the time of measurement. We also show the MP and BS models (Equations 1 and 2) for average SW conditions.

### 2.1. Estimating the Magnetosheath Geometry

The MSH is often classified by its geometry through the shock normal angle $\theta_{Bn}$. We estimate $\theta_{Bn}$ using semi-empirical models for the magnetopause (MP) and BS depending solely on upstream parameters, that is, not constrained by observed MP or BS crossings. For the MP, we use the Shue et al. (1998) model for the radial distance $r$ at an angle $\vartheta$ to the Sun-Earth line:

$$r = r_0 \left( \frac{2}{1 + \cos \vartheta} \right)^{\alpha}. \tag{1}$$

The MP standoff distance $r_0$ and tail flaring $\alpha$ depend on the solar wind dynamic pressure and $z$ component of the IMF; see Equations 10 and 11 in Shue et al. (1998) for complete expressions. We use a parabolic BS model (Merka et al., 2003):

$$X_{GSE} = a_s - b_s \left( Y_{GSE}^2 + Z_{GSE}^2 \right), \tag{2}$$

where $(X_{GSE}, Y_{GSE}, Z_{GSE})$ are the GSE (Geocentric Solar Ecliptic) coordinates of the shock surface. The BS standoff distance $a_s$ (Farris & Russell, 1994) and the flaring parameter $b_s$ (Fairfield et al., 2001) are functions of $r_0$, $\alpha$, the upstream dynamic pressure, and Alfvénic and fast mode Mach numbers. We retrieve the upstream magnetic field vector $\boldsymbol{B}_{SW}$, proton density $n_{SW}$, speed $V_{SW}$, and temperature $T_{SW}$ at a one-minute time resolution from the OMNI database (Papitashvili & King, 2020) with data from the Wind and ACE spacecraft. We traced the MMS location along $X_{GSE}$ to the surface defined by Equation 2 (i.e., assumed the same $(Y_{GSE}, Z_{GSE})$ at the BS and



21699402, 2025, 1, Downloaded from https://agupubs.onlinelibrary.wiley.com/doi/10.1029/2024JA033272 by University Of Helsinki, Wiley Online Library on [03/03/2025]. See the Terms and Conditions (https://onlinelibrary.wiley.com/terms-and-conditions) on Wiley Online Library for rules of use; OA articles are governed by the applicable Creative Commons License

the spacecraft) and calculated the model shock normal direction $\hat{n}$ at that point (see Figure 1). We then calculated $\theta_{Bn}$ as the angle between $\hat{n}$ and $\boldsymbol{B}_{SW}$.

The upstream measurements from the OMNI database are made by spacecraft near L1 and propagated to the BS nose using a time lag $\Delta t_{SW}$, typically around 45 min, determined by the ion bulk speed. Variable solar wind speed or quick changes in the IMF direction may introduce errors in $\Delta t_{SW}$ and the $\theta_{Bn}$ calculation. For each 30-s interval in our analysis, we define a window with a length of the RMS (root mean square) of $\Delta t_{SW}$. We consider $\theta_{Bn}$ reliably determined if the OMNI data coverage is at least 80 % and the estimated $\theta_{Bn}$ changes less than 20° during this window. In intervals that do not meet these conditions, $\theta_{Bn}$ is undetermined and not included in the results. While some uncertainty is expected for the remaining intervals, we can still study the average dependencies on $\theta_{Bn}$.

From our model MP (Equation 1) and BS (Equation 2), we also calculate the MMS location relative to these boundaries as the fractional distance $d_{MP-BS}$ (Dimmock & Nykyri, 2013):

$$d_{MP-BS} = \frac{|\boldsymbol{R}_{MMS}| - |\boldsymbol{r}_{MP}|}{|\boldsymbol{r}_{BS}| - |\boldsymbol{r}_{MP}|}, \tag{3}$$

where $\boldsymbol{R}_{MMS}$ is the GSE location of MMS and $\boldsymbol{r}_{MP}$ and $\boldsymbol{r}_{BS}$ are points on the MP and BS, respectively, for the same angle $\vartheta$ as $\boldsymbol{R}_{MMS}$ (see Figure 1). As it can be readily seen in Equation 3, when MMS is located at the MP, $d_{MP-BS} = 0$, while $d_{MP-BS} = 1$ for locations at the BS. Values just outside this range exist due to uncertainty in the model boundaries, and we adjust this so that $d_{MP-BS} \gtrsim 1 \rightarrow d_{MP-BS} = 1$ and $d_{MP-BS} \lesssim 0 \rightarrow d_{MP-BS} = 0$.

### 2.2. Local Magnetosheath Parameters

We investigate the use of local measurements to classify the MSH as an alternative to $\theta_{Bn}$. In Figure 2, we show a MSH interval from 20 March 2023 which displays different MSH behaviors. The first three panels are based on L1 measurements from the OMNI database: solar wind magnetic field $\boldsymbol{B}_{SW}$ (Figure 2a), solar wind speed $V_{SW}$ (Figure 2b), and shock normal angle $\theta_{Bn}$ (Figure 2c). Figures 2d–2j show MMS measurements. MMS is in the MSH between ∼00:55 and ∼04:45 UTC, as seen by the increased magnetic field compared to the solar wind (Figure 2d), high density $n_i$ (Figure 2e), and lower speed than in the solar wind (ion velocity $\boldsymbol{V}_i$ in Figure 2f). The omnidirectional ion differential energy flux (DEF) (Figure 2g) is used to differentiate the MSH plasma (warm, broad energy distribution) from the solar wind (monoenergetic beam seen before 00:55) and magnetosphere (high-energy ions visible after 04:45).

To investigate the local classification of the MSH, we use the parameters defined in Karlsson et al. (2021). We divide our data into 30-s intervals, and for each interval we quantify the magnetic fluctuations, ion temperature anisotropy, and suprathermal ion flux. We compute the magnetic fluctuation level by calculating the standard deviation during each 30-s MSH interval in the magnetic field components:

$$\sigma_{30s}(\boldsymbol{B}) = \sqrt{\sigma_{30s}(B_x)^2 + \sigma_{30s}(B_y)^2 + \sigma_{30s}(B_z)^2}. \tag{4}$$

We show $\sigma_{30s}(\boldsymbol{B})$ computed with 30-s moving standard deviation in Figure 2h. An alternative, which we also explore, is to normalize $\sigma_{30s}(\boldsymbol{B})$ to the mean magnetic field strength during the 30-s window ($\langle B \rangle$) obtaining the dimensionless parameter $\tilde{\sigma}_B \equiv \sigma_{30s}(\boldsymbol{B})/\langle B \rangle$ (not shown in Figure 2). In Figure 2i we show the ion temperature anisotropy which is given by

$$A_i = \frac{T_{i\perp}}{T_{i\parallel}} - 1, \tag{5}$$

such that $A_i = 0$ corresponds to an isotropic ion velocity distribution. Figure 2j shows the energetic ion flux $F_{high}$, defined as the integral of the omnidirectional ion DEF from FPI in the spacecraft measurement frame. The four highest energy channels on FPI are centered at $E_{i1,2,3,4} = (17.8, 13.7, 10.5, 8.1)$ keV and have widths $\Delta E_{i1,2,3,4} = (4.7, 3.6, 2.8, 2.1)$ keV. We integrate over the three highest energy channels which include energies above ∼9 keV, close to the limit used in Karlsson et al. (2021):



21699402, 2025, 1, Downloaded from https://agupubs.onlinelibrary.wiley.com/doi/10.1029/2024JA033272 by University Of Helsinki, Wiley Online Library on [03/03/2025]. See the Terms and Conditions (https://onlinelibrary.wiley.com/terms-and-conditions) on Wiley Online Library for rules of use; OA articles are governed by the applicable Creative Commons License

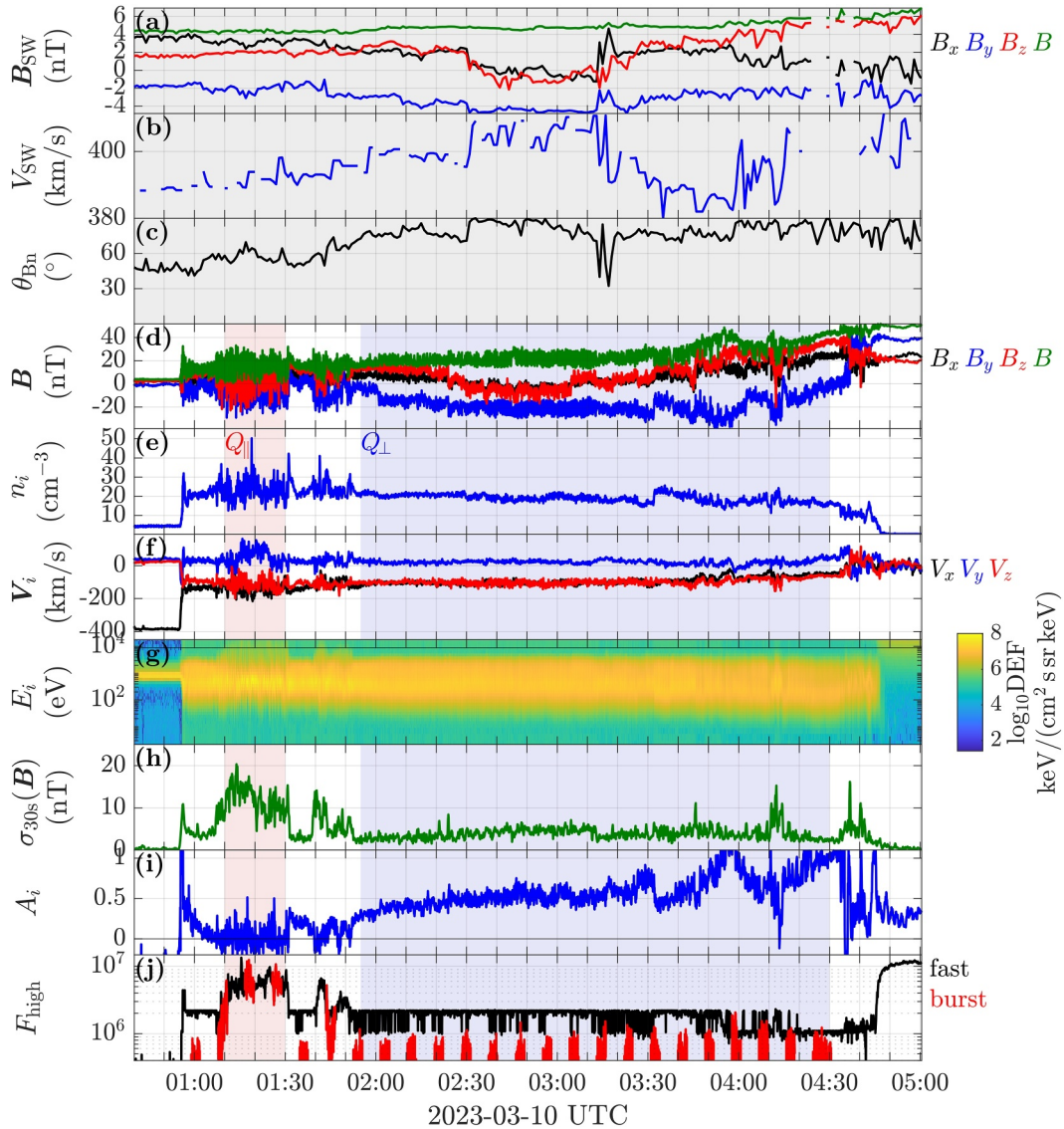



**Figure 2.** Example of a MSH crossing from the unbiased MSH campaign. Panels (a)–(c) are based on Wind measurements at L1 propagated to the bow shock: (a) Solar wind magnetic field $\boldsymbol{B}_{SW}$. (b) Solar wind bulk speed $V_{SW}$. (c) Shock normal angle $\theta_{Bn}$. (d)–(j) MMS measurements: (d) Magnetic field $\boldsymbol{B}$. (e) Ion density $n_i$. (f) Ion bulk velocity $\boldsymbol{V}_i$. (g) Ion omnidirectional differential energy flux, fast data. The horizontal black line at ∼9 keV indicates the energy above which $F_{high}$ is calculated. (h) Magnetic fluctuation level $\sigma_{30s}(\boldsymbol{B})$ in nT. (i) Ion temperature anisotropy $A_i$. (j) Energetic ion flux $F_{high}$ in units keV/(cm$^2$ s sr), using fast data (black) and burst data (red). Red and blue shade in (d)–(j) indicate where the MSH displays features typical for the $Q_\parallel$ and $Q_\perp$ MSH, respectively.

$$F_{high} = \sum_{n=1,2,3} \mathrm{DEF}(E_{in})\Delta E_{in}. \quad (6)$$

In Figure 2j, $F_{high}$ is computed with both fast (black) and burst (red) data. Note that $F_{high}$ computed from fast data is consistently higher than that from burst data except for around 01:10-01:30. With fast data, $F_{high}$ is overestimated due to the on-board data compression described in Section 2.2.1.

Early, around 01:10-01:30 (red shaded interval in Figures 2d–2j), the MSH has stronger fluctuations in $\boldsymbol{B}$, $n_i$, and $\boldsymbol{V}_i$, $A_i \approx 0$, and higher $F_{high}$, that is, features typical for the $Q_\parallel$ MSH, compared to later in the interval. After 01:50 (blue shaded interval), the MSH transitions into a typical $Q_\perp$ state with lower fluctuations, higher $A_i$ and lower



21699402, 2025, 1, Downloaded from https://agupubs.onlinelibrary.wiley.com/doi/10.1029/2024JA033272 by University Of Helsinki, Wiley Online Library on [03/03/2025]. See the Terms and Conditions (https://onlinelibrary.wiley.com/terms-and-conditions) on Wiley Online Library for rules of use; OA articles are governed by the applicable Creative Commons License

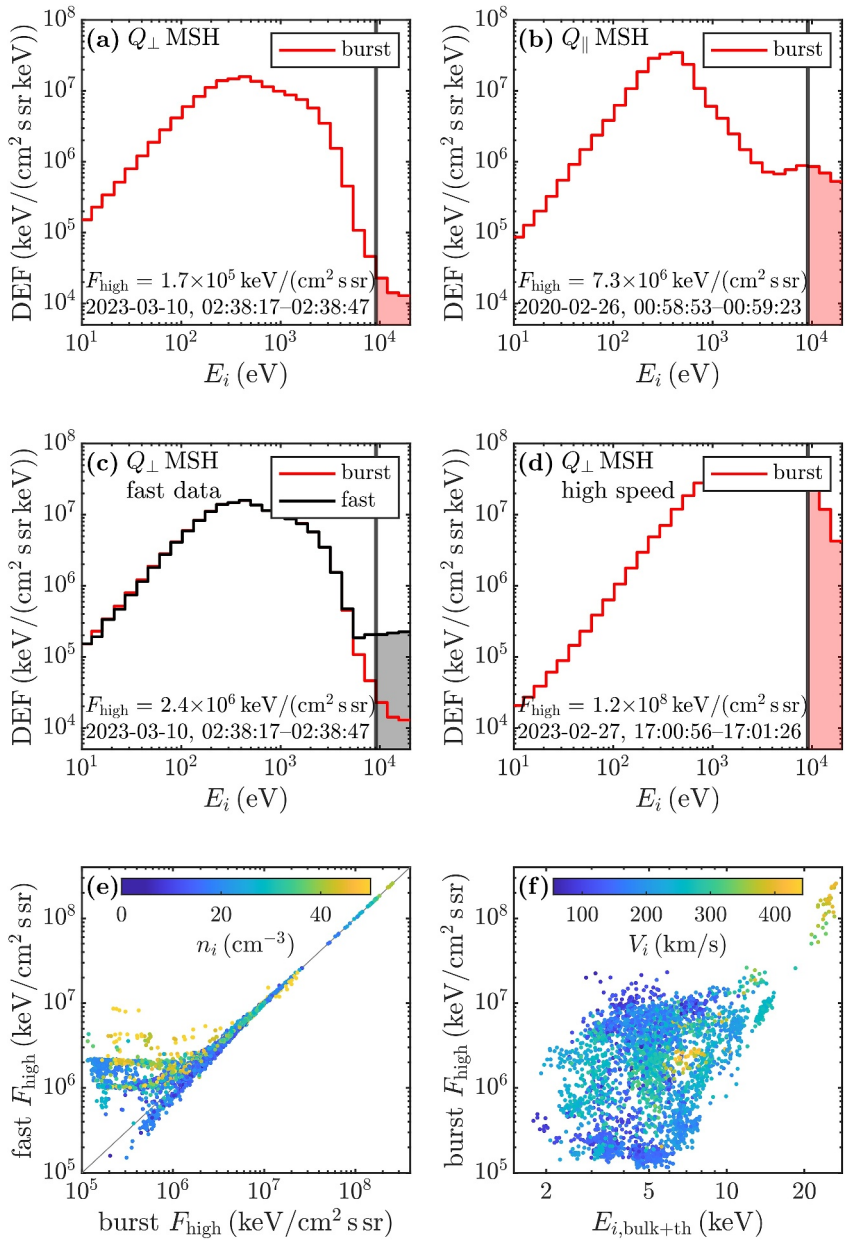



**Figure 3.** Example ion distributions showing $F_{high}$ as the integrated shaded area above 9 keV (vertical line). (a) Typical $Q_\perp$ MSH. (b) Typical $Q_\parallel$ MSH. (c) Typical $Q_\perp$ MSH (same as (a)), red curve showing burst and black showing fast data. Here, $F_{high}$ is calculated from fast data which gives a larger value than in (a). (d) High-speed MSH. (e) $F_{high}$ from our whole data set calculated with burst and fast data, averaged in 30-s windows. Color shows ion density $n_i$. (f) $F_{high}$ from burst data versus the bulk thermal energy $E_{i,bulk+th}$. Color shows ion bulk speed $V_i$.

$F_{high}$. The change in the local parameters is accompanied by a higher $\theta_{Bn}$ than at the start of the interval; however, there is no direct correspondence between changes in $\theta_{Bn}$ and the change in local plasma parameters. For example, $\theta_{Bn}$ decreases slightly from 01:10 to 01:40 while the local parameters transition into a typical $Q_\perp$ state. Also, the dip in $\theta_{Bn}$ at 03:10-03:20 shows no signature in the local MSH parameters. Figure 2 exemplifies that features typical for the $Q_\parallel$ MSH can exist for an estimated $\theta_{Bn}$ up to ~70°. There is also an uncertainty in $\theta_{Bn}$ caused by potential OMNI propagation errors.

Figure 3a shows an example of $F_{high}$ calculated in the $Q_\perp$ MSH without an energetic tail in the ion distribution, giving $F_{high} = 1.7 \times 10^5$ keV/(cm$^2$ s sr). Figure 3b shows an example from the $Q_\parallel$ MSH, where the ion



21699402, 2025, 1, Downloaded from https://agupubs.onlinelibrary.wiley.com/doi/10.1029/2024JA033272 by University Of Helsinki, Wiley Online Library on [03/03/2025]. See the Terms and Conditions (https://onlinelibrary.wiley.com/terms-and-conditions) on Wiley Online Library for rules of use; OA articles are governed by the applicable Creative Commons License

21699402, 2025, 1, Downloaded from https://agupubs.onlinelibrary.wiley.com/doi/10.1029/2024JA033272 by University Of Helsinki, Wiley Online Library on [03/03/2025]. See the Terms and Conditions (https://onlinelibrary.wiley.com/terms-and-conditions) on Wiley Online Library for rules of use; OA articles are governed by the applicable Creative Commons License

distribution has an energetic tail, resulting in the higher value $F_{\text{high}} = 7.3 \times 10^6$ keV/(cm$^2$ s sr). In $F_{\text{high}}$ all ions with energy above ∼9 keV in the measurement frame are counted as suprathermal, which allows for a quick classification. However, we have identified two caveats that should be considered, described in the next subsections.

#### 2.2.1. Data Compression Effects On-Board MMS

The unprecedented measurement cadence and resolution of MMS puts a high demand on the amount of data to be downlinked to Earth. One necessary measure is to reduce the size of the data using on-board compression, which can artificially increase $F_{\text{high}}$.

The full 3D ion distributions measured by FPI (so-called sky maps) are treated as images consisting of 32 columns (azimuth) and 512 rows (32 energy and 16 elevation bins). The image is compressed using a discrete wavelet transform which removes noise and small-scale features while preserving the larger features of the image. Barrie et al. (2017) explored several effects of wavelet truncation on the FPI sky maps, one of which being an *elevated noise floor* which removes all information about the distribution at low count rates. This poses a problem since detecting the presence or absence of high-energy ions requires low-count measurements.

For the burst data, the compression is usually lossless, that is, the wavelets are not truncated except at high densities above ∼100 cm$^{-3}$ (Barrie et al., 2019). The fast survey maps are created by summing uncompressed burst maps during a window of 4.5 s. Therefore a fast survey map contains roughly 30 times the counts of a burst map, and is subject to more truncation and potentially larger compression errors. Figure 3c shows the same ion distribution as Figure 3a, that is, from the $Q_\perp$ MSH without a suprathermal tail. The burst-mode distribution (red) drops off at high energies while the fast-mode distribution (black) remains at a constant value, revealing the elevated noise floor caused by data compression. This results in $F_{\text{high}} = 2.4 \times 10^6$ keV/(cm$^2$ s sr) (black shaded area), a value more typical for the $Q_\parallel$ MSH (see e.g., Figure 3b). In Figure 3e, we compare the burst and fast values of $F_{\text{high}}$ for all intervals in our data set. At burst-mode $F_{\text{high}} \lesssim 5 \times 10^6$ keV/(cm$^2$ s sr), the fast-mode values are often significantly higher than the burst. The compression error increases with density, as those distributions typically have higher counts. This artificial increase in $F_{\text{high}}$ makes the fast-mode data from MMS unfit to reliably detect high-energy ions in the MSH.

#### 2.2.2. High-Speed and High-Temperature Effect on $F_{\text{high}}$

The calculation of $F_{\text{high}}$ in this and previous works (Karlsson et al., 2021; Koller et al., 2024; Raptis et al., 2020) is done in the spacecraft rest frame. If the ion bulk speed is high, however, the ion rest frame significantly deviates from the spacecraft frame. In Figure 3d, we show such an example where the bulk distribution is shifted to a higher energy into the integration interval resulting in the high value $F_{\text{high}} = 1.2 \times 10^8$ keV/(cm$^2$ s sr). Here, $F_{\text{high}}$ includes part of the ion bulk distribution and does not correctly capture the suprathermal ion population. Similar effects are expected if the ion temperature is very high so that the thermal energy becomes comparable to the integration limit. To find an upper limit on $V_i$ and $T_i$ where $F_{\text{high}}$ is reliable, we define the bulk thermal energy as

$$E_{i,\text{bulk+th}} = \frac{1}{2} m_i (V_i + 4V_{i\text{th}})^2, \tag{7}$$

where $V_i$ is the ion bulk speed, $m_i$ the proton mass, $V_{i\text{th}} = \sqrt{2T_i/m_i}$ is the ion thermal speed, and $T_i$ is the ion temperature. At $4V_{i\text{th}}$, a Maxwellian distribution has dropped to $10^{-7}$ times its maximum value, which puts $E_{i,\text{bulk}+\text{th}}$ in the end of the thermal part of the distribution. The ion bulk speed $V_i$ gives the shift from the spacecraft frame. Figure 3f shows $F_{\text{high}}$ as a function of $E_{i,\text{bulk}+\text{th}}$ for all intervals in our data set. When $E_{i,\text{bulk}+\text{th}} > 6$ keV, the lowest $F_{\text{high}}$ increases with increasing $E_{i,\text{bulk}+\text{th}}$. Here, the thermal ion population enters the integration interval for $F_{\text{high}}$, and more than the suprathermal tail is captured. The highest values $F_{\text{high}} > 10^8$ keV/(cm$^2$ s sr) are caused by very high speeds above 400 km/$s$. When presenting the results in Section 3, we only include $F_{\text{high}}$ when $E_{i,\text{bulk}+\text{th}} < 6$ keV.

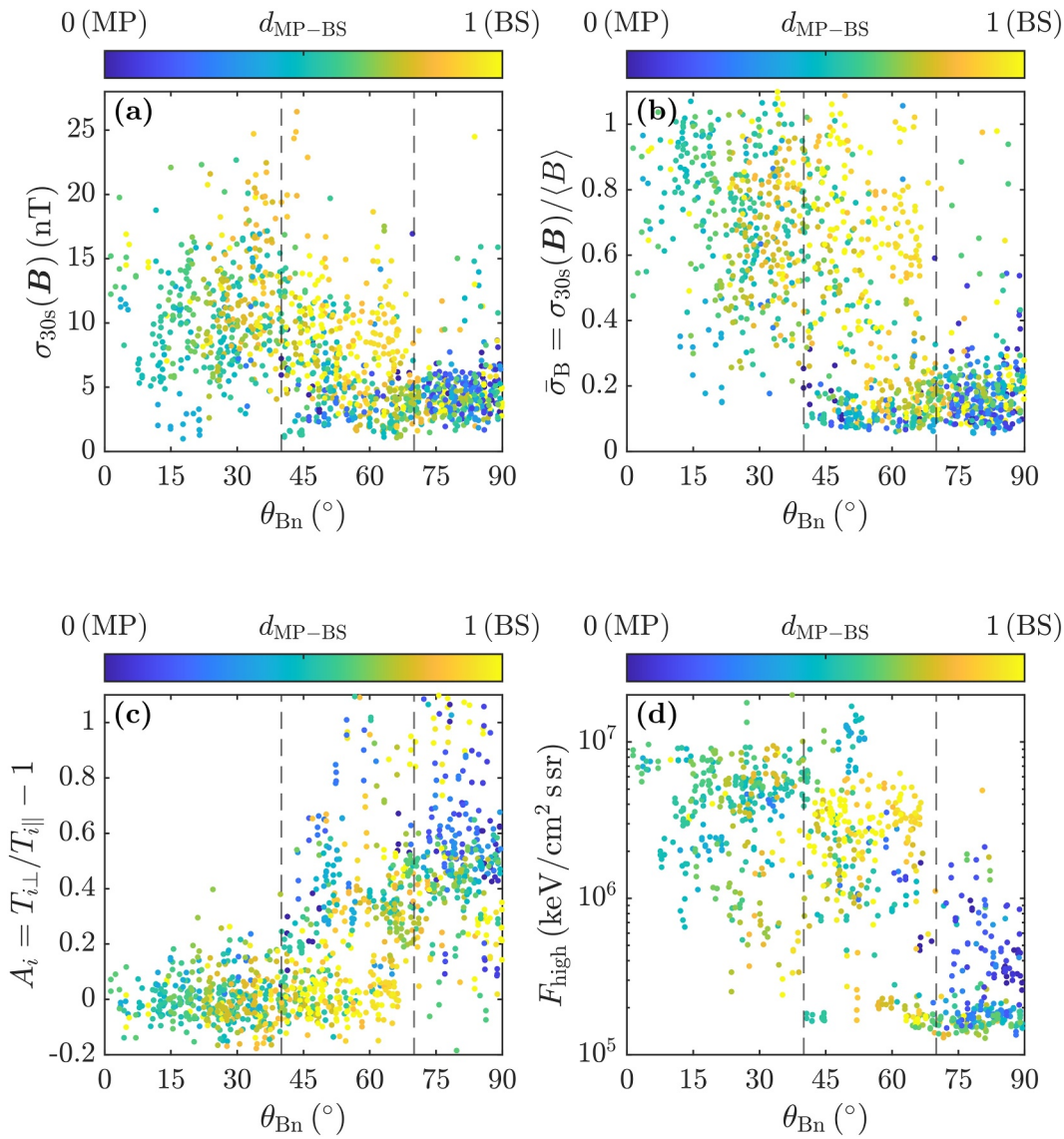



**Figure 4.** Local parameters versus $\theta_{\mathrm{Bn}}$ in intervals where $\theta_{\mathrm{Bn}}$ could be determined. (a) Magnetic fluctuation level $\sigma_{30s}(\boldsymbol{B})$ in nT. (b) Normalized magnetic fluctuation level $\bar{\sigma}_B$. (c) Ion temperature anisotropy $A_i$. (d) Energetic ions, $F_{\mathrm{high}}$, calculated from burst-mode data and only including points where $E_{i,\mathrm{bulk+th}} < 6$ keV. The color scale shows the fractional distance $d_{\mathrm{MP-BS}}$ and the two dashed vertical lines indicate $\theta_{\mathrm{Bn}} = 40°$ and 70°.

## 3. Results

### 3.1. Local Parameter Dependence on Magnetosheath Geometry

We now investigate how the local MSH parameters depend on the shock normal angle $\theta_{\mathrm{Bn}}$ and the location in the MSH. In Figures 4a–4d, we show $\sigma_{30s}(\boldsymbol{B})$, $\bar{\sigma}_B$, $A_i$, and $F_{\mathrm{high}}$ as a function of $\theta_{\mathrm{Bn}}$ in the intervals where $\theta_{\mathrm{Bn}}$ could be determined (see Section 2.1). The color scale shows the fractional distance $d_{\mathrm{MP-BS}}$ (Equation 3).

The magnetic fluctuations (Figure 4a) are stronger ($\sigma_{30s}(\boldsymbol{B}) \sim 10$ nT) for $\theta_{\mathrm{Bn}} < 40°$, and weaker ($\sigma_{30s}(\boldsymbol{B}) \sim 4$ nT) for $\theta_{\mathrm{Bn}} > 70°$. There is a trend; however, there is no clear separation between high and low $\sigma_{30s}(\boldsymbol{B})$ as intermediate fluctuation levels of ~5 nT appear across all values of $\theta_{\mathrm{Bn}}$. It makes sense to normalize the magnetic field fluctuations considering the variability of the upstream conditions. Indeed, as Figure 4b shows, the high and low fluctuation levels are better separated with $\bar{\sigma}_B$. We find $\bar{\sigma}_B \sim 0.4$-1 for $\theta_{\mathrm{Bn}} < 40°$, and $\bar{\sigma}_B < 0.3$ for $\theta_{\mathrm{Bn}} > 70°$. In



21699402, 2025, 1, Downloaded from https://agupubs.onlinelibrary.wiley.com/doi/10.1029/2024JA033272 by University Of Helsinki, Wiley Online Library on [03/03/2025]. See the Terms and Conditions (https://onlinelibrary.wiley.com/terms-and-conditions) on Wiley Online Library for rules of use; OA articles are governed by the applicable Creative Commons License

21699402, 2025, 1, Downloaded from https://agupubs.onlinelibrary.wiley.com/doi/10.1029/2024JA033272 by University Of Helsinki, Wiley Online Library on [03/03/2025]. See the Terms and Conditions (https://onlinelibrary.wiley.com/terms-and-conditions) on Wiley Online Library for rules of use; OA articles are governed by the applicable Creative Commons License

both panels, there is an overlap of high and low fluctuation levels at $\theta_{Bn}$ between approximately 40° and 70° (dashed vertical lines).

Considering $A_i$ (Figure 4c), the ion temperature is mostly isotropic ($A_i \approx 0$) for $\theta_{Bn} < 40°$. For $\theta_{Bn} > 70°$, we find higher values and also a large spread, with higher $A_i$ closer to the MP ($d_{MP-BS} \approx 0$; blue) than closer to the BS ($d_{MP-BS} \approx 1$; yellow). We again observe an overlap in $\theta_{Bn} \in [40°, 70°]$ containing both high and low values of $A_i$.

We detect suprathermal ions, $F_{high} \gtrsim 10^6$ keV/(cm$^2$ s sr), in most intervals with $\theta_{Bn} < 70°$ (see Figure 4d). The overlap region, $\theta_{Bn} \in [40°, 70°]$, is less pronounced for $F_{high}$ than for $\tilde{\sigma}_B$ and $A_i$. For $\theta_{Bn} > 70°$, the main population of $F_{high}$ lies below $\sim 3 \times 10^5$ keV/(cm$^2$ s sr), but some intervals are reaching higher values up to $\sim 10^6$ keV/(cm$^2$ s sr). We note that these intervals mainly lie close to the MP ($d_{MP-BS} < 0.25$, dark blue). For the $\theta_{Bn} < 70°$ intervals, we observe an order of magnitude lower $F_{high}$ at the flanks, with $F_{high} \sim 10^6$ keV/(cm$^2$ s sr) at $|Y_{GSE}| \approx 20 R_E$ compared to $F_{high} \sim 10^7$ keV/(cm$^2$ s sr) at $|Y_{GSE}| \approx 0$ (see Figure S1 in Supporting Information S1). Our values of $F_{high}$ are lower by a factor of $10^3$ than those reported by Karlsson et al. (2021) and Koller et al. (2024) due to a unit conversion error in these works.

The MMS measurements presented here show that the $Q_\parallel$ MSH is typically associated with stronger magnetic fluctuations, lower ion temperature anisotropy, and more energetic ions than the $Q_\perp$ MSH, in agreement with previous works based on data from other spacecraft. The trends in all our parameters are consistent with the similar Cluster study by Karlsson et al. (2021). We have also found that the transition in local properties is not sharp at a given angle $\theta_{Bn}$, but rather that the MSH in the interval $\theta_{Bn} \in [40°, 70°]$ can have features typical of either $Q_\parallel$ MSH or $Q_\perp$ MSH, in line with Karlsson et al. (2021). As notation for these two MSH categories determined from local parameters, we will henceforth use $\tilde{Q}_\parallel$ for $Q_\parallel$-like MSH (high-$\tilde{\sigma}_B$, low-$A_i$, high-$F_{high}$) and $\tilde{Q}_\perp$ for $Q_\perp$-like MSH (low-$\tilde{\sigma}_B$, high-$A_i$, low-$F_{high}$).

### 3.2. Distributions of Local Parameters

We now explore whether the local parameters defined in Section 2.2 are suitable to separate the MSH into the two distinct regimes $\tilde{Q}_\parallel$ and $\tilde{Q}_\perp$, with the goal of obtaining a classification that does not rely on the knowledge of upstream conditions. As reasoned by Koller et al. (2024), a suitable parameter should display a double-peaked distribution to properly separate two distinct configurations. In Figures 5a–5d, we show histograms of $\sigma_{30s}(\boldsymbol{B})$, $\tilde{\sigma}_B$, $A_i$, and $F_{high}$ from the full data set. In Figures 5e–5h, we show the same parameters as in Figures 5a–5d but we further distinguish them depending on the model-calculated $\theta_{Bn}$ with three ranges based on Figure 4, plotted in red ($\theta_{Bn} < 40°$), blue ($\theta_{Bn} > 70°$), and light gray ($40° \leq \theta_{Bn} \leq 70°$). The full distributions (gray) have fewer counts than the distributions shown in Figures 5a–5d since we exclude from the data set the intervals where $\theta_{Bn}$ cannot be determined.

In Figure 5a, we show the magnetic fluctuation level $\sigma_{30s}(\boldsymbol{B})$. We observe a single distribution that does not reveal two separate regimes. Below (Figure 5e), we see that $\theta_{Bn} < 40°$ has on-average stronger fluctuations than $\theta_{Bn} > 70°$, but that the peaks are not distinguishable without knowledge of the upstream conditions. In contrast, $\tilde{\sigma}_B$ has two populations peaked at ~0.1 ($\tilde{Q}_\perp$ MSH) and ~0.8 ($\tilde{Q}_\parallel$ MSH). In Figure 5f, we see that almost all $\theta_{Bn} > 70°$ (blue) intervals are included in the low-$\tilde{\sigma}_B$ peak and that the $\theta_{Bn} < 40°$ (red) intervals form the high-$\tilde{\sigma}_B$ peak. The transition from $\tilde{Q}_\perp$ to $\tilde{Q}_\parallel$ (i.e., the intersection of the blue and red lines) occurs at $\tilde{\sigma}_B \approx 0.3$. In Figure 5c, $A_i$ has one sharp peak at $A_i = 0$ ($\tilde{Q}_\parallel$ MSH) and a broad shoulder at higher $A_i$ ($\tilde{Q}_\perp$ MSH). We interpret this as two partly overlapping populations. The transition from $\tilde{Q}_\parallel$ to $\tilde{Q}_\perp$ occurs at $A_i \approx 0.2$ (Figure 5g).

We also observe a double-peaked distribution in $F_{high}$ in Figure 5d. Here, we use burst data and include only intervals where $E_{i,bulk+th} < 6$ keV (see Section 2.2.2). There is a sharp peak at $F_{high} \approx 2 \times 10^5$ keV/(cm$^2$ s sr) ($\tilde{Q}_\perp$ MSH), where the suprathermal ion flux is at noise level or very low, and a broader one at $F_{high} \approx 5 \times 10^6$ keV/(cm$^2$ s sr) ($\tilde{Q}_\parallel$ MSH). In Figure 5h, we see that the $\theta_{Bn} > 70°$ intervals (blue) reach $F_{high}$ up to $10^6$ keV/(cm$^2$ s sr), where the higher values of $F_{high} \gtrsim 3 \times 10^5$ keV/(cm$^2$ s sr) are found close to the MP ($d_{MP-BS} < 0.25$; see Figure 4d). Among the oblique ($40° \leq \theta_{Bn} \leq 70°$) intervals (light gray, Figures 5e–5h), there exist features from both peaks.

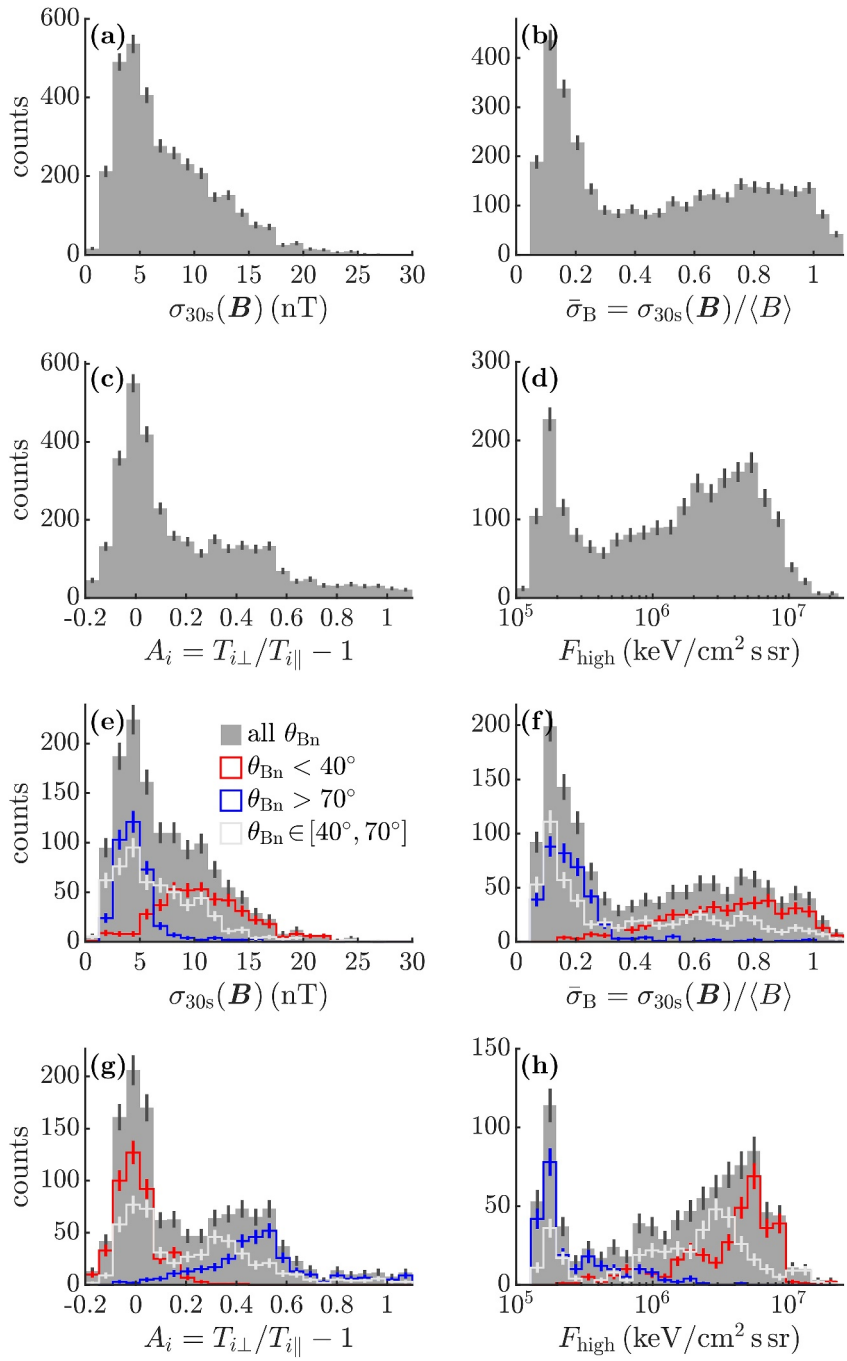



**Figure 5.** Distributions of local MSH parameters in our data set. (a) Magnetic fluctuation level $\sigma_{30s}(\boldsymbol{B})$. (b) Normalized magnetic fluctuation level $\bar{\sigma}_B$. (c) Ion temperature anisotropy $A_i$. (d) Suprathermal ion population $F_{high}$ calculated from burst-mode data and only including points where $E_{i,bulk+th} < 6$ keV. Panels (e)–(h) same parameters as in (a)–(d), with the distributions from three $\theta_{Bn}$ ranges overplotted: red for $\theta_{Bn} < 40°$, light gray for $40° \leq \theta_{Bn} \leq 70°$, and blue for $\theta_{Bn} > 70°$. For (e)–(h), we include only intervals where $\theta_{Bn}$ could be determined. We have verified that the histogram shapes are insensitive to a change in the bin width by a factor of two. The error bars are estimated by the standard Poisson error $\sqrt{N}$, where $N$ is the counts in each bin.

In summary, we find that the local MSH parameters $\bar{\sigma}_B$, $A_i$, and $F_{high}$ individually separate the MSH into two configurations by displaying double-peaked distributions. The distributions are also consistent with the model-estimated $\theta_{Bn}$.



21699402, 2025, 1, Downloaded from https://agupubs.onlinelibrary.wiley.com/doi/10.1029/2024JA033272 by University Of Helsinki, Wiley Online Library on [03/03/2025]. See the Terms and Conditions (https://onlinelibrary.wiley.com/terms-and-conditions) on Wiley Online Library for rules of use; OA articles are governed by the applicable Creative Commons License

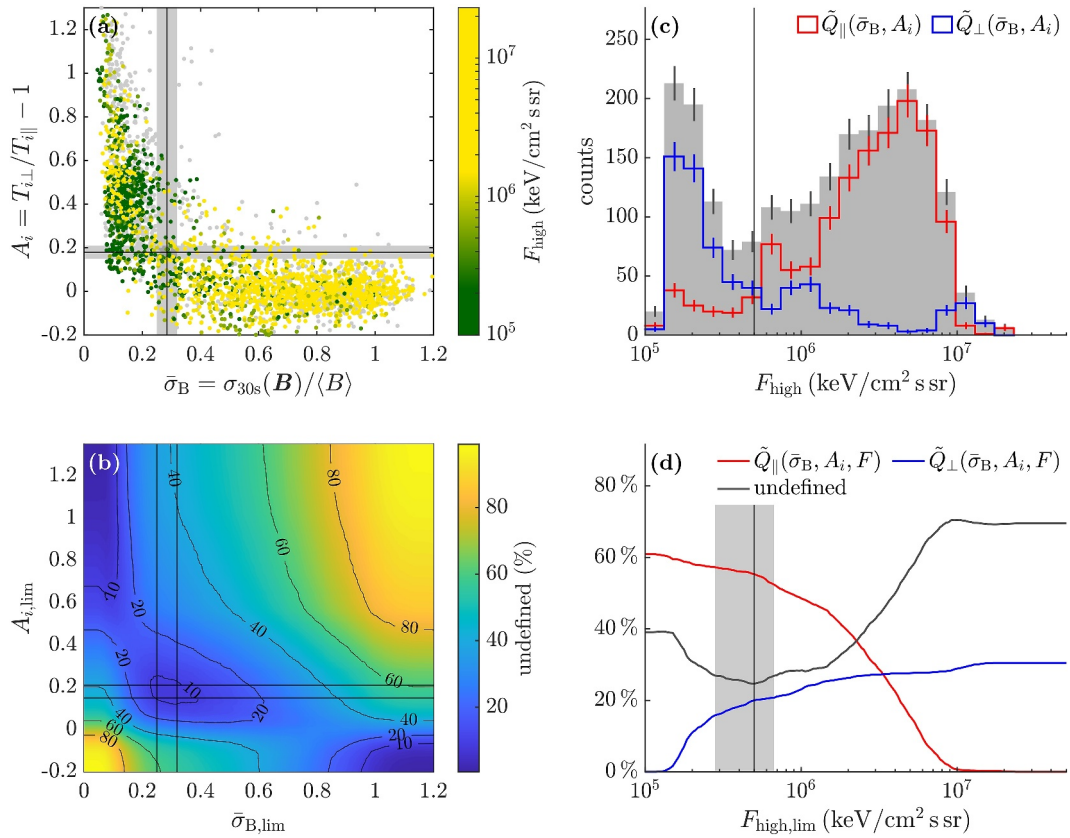



**Figure 6.** (a) Scatter plot of $\bar{\sigma}_B$ versus $A_i$. The color scale shows $F_{high}$ where $E_{i,bulk+th} < 6$ keV. The gray points correspond to higher values of $E_{i,bulk+th}$. (b) Percentage of undefined intervals (Equation 8) as a function of $\bar{\sigma}_{B,lim}$ and $A_{i,lim}$. (c) Distribution of $F_{high}$ in the whole MSH (gray), and in intervals labeled as $\tilde{Q}_\parallel$ (red) and $\tilde{Q}_\perp$ (blue) by $\bar{\sigma}_B$ and $A_i$. The error bars are estimated by the standard Poisson error $\sqrt{N}$, where $N$ is the counts in each bin. (d) Percentage of $\tilde{Q}_\parallel$ (red), $\tilde{Q}_\perp$ (blue), and undefined (gray) intervals (Equation 9) as a function of $F_{high,lim}$.

### 3.3. Identifying Limits on the Local Parameters

We now want to find the optimal thresholds in the local parameters to separate the MSH into two categories. We choose not to optimize based on $\theta_{Bn}$ due to uncertainty in the model estimation and the variation of the position of the foreshock edge leading to the overlap range $(40° \leq \theta_{Bn} \leq 70°)$. We instead find the threshold values that maximize the number of MSH intervals that are consistently categorized into either $\tilde{Q}_\parallel$ (high-$\bar{\sigma}_B$/low-$A_i$/high-$F_{high}$) or $\tilde{Q}_\perp$ (low-$\bar{\sigma}_B$/high-$A_i$/low-$F_{high}$), thereby minimizing the number of undefined intervals. The $\tilde{Q}$ notation emphasizes that the classification is based on local parameters and not the shock geometry $\theta_{Bn}$ based on upstream parameters.

In Figure 6a, we show $\bar{\sigma}_B$ and $A_i$ for the same data set as in Figures 5a–5d. Most of the intervals are ordered into either the top left (low-$\bar{\sigma}_B$/high-$A_i$) corner typical for the $\tilde{Q}_\perp$ MSH, or the bottom right (high-$\bar{\sigma}_B$/low-$A_i$) corner typical for the $\tilde{Q}_\parallel$ MSH. The colors show $F_{high}$ with green and yellow approximately corresponding to the low- and high-$F_{high}$ populations identified in Figure 5d. Gray corresponds to $E_{i,bulk+th} > 6$ keV, where $F_{high}$ does not correctly quantify the suprathermal ions (see Section 2.2.2). The lower right corner consists mainly of high-$F_{high}$ intervals (yellow), that is, $\tilde{Q}_\parallel$ MSH, consistent with $\bar{\sigma}_B$ and $A_i$. In the top left corner, we mainly observe low values of $F_{high}$, that is, $\tilde{Q}_\perp$ MSH, but there are also some high-$F_{high}$ intervals ($\sim 10^7$ keV/$\left(\text{cm}^2\ \text{s sr}\right)$; yellow). These come from the 24 March 2023 when a coronal mass ejection (CME) impacted the MSH while MMS was in the subsolar region $(|Y_{GSE}| < 1.5R_E)$, seeing a highly compressed MSH with $n_i \sim 70$ cm$^{-3}$, $B \approx 60$ nT.



21699402, 2025, 1, Downloaded from https://agupubs.onlinelibrary.wiley.com/doi/10.1029/2024JA033272 by University Of Helsinki, Wiley Online Library on [03/03/2025]. See the Terms and Conditions (https://onlinelibrary.wiley.com/terms-and-conditions) on Wiley Online Library for rules of use; OA articles are governed by the applicable Creative Commons License

21699402, 2025, 1, Downloaded from https://agupubs.onlinelibrary.wiley.com/doi/10.1029/2024JA033272 by University Of Helsinki, Wiley Online Library on [03/03/2025]. See the Terms and Conditions (https://onlinelibrary.wiley.com/terms-and-conditions) on Wiley Online Library for rules of use; OA articles are governed by the applicable Creative Commons License

**Table 1**
*Limits in the Local Parameters to Distinguish Between $\tilde{Q}_{\parallel}$ and $\tilde{Q}_{\perp}$*

| MSH type | Definition | Number of intervals |
|---|---|---|
| All intervals | | 3,292 (100%) |
| $\tilde{Q}_{\parallel}(\bar{\sigma}_B, A_i)$ | $\bar{\sigma}_B > 0.29$ & $A_i < 0.18$ | 1,789 (54.3%) |
| $\tilde{Q}_{\perp}(\bar{\sigma}_B, A_i)$ | $\bar{\sigma}_B < 0.29$ & $A_i > 0.18$ | 1,213 (36.9%) |
| Undefined | | 290 (8.8%) |
| All intervals using $F_{high}$ | | 2,254 (100%) |
| $\tilde{Q}_{\parallel}(\bar{\sigma}_B, A_i, F)$ | $\tilde{Q}_{\parallel}(\bar{\sigma}_B, A_i)$ & $F_{high} > 5 \times 10^5$ keV/(cm$^2$ s sr) | 1,247 (55.3%) |
| $\tilde{Q}_{\perp}(\bar{\sigma}_B, A_i, F)$ | $\tilde{Q}_{\perp}(\bar{\sigma}_B, A_i)$ & $F_{high} < 5 \times 10^5$ keV/(cm$^2$ s sr) | 451 (20.0%) |
| Undefined | | 556 (24.7%) |

We start by establishing threshold values in $\bar{\sigma}_B$ and $A_i$, since $F_{high}$ is only reliable for part of the data set. We group all the MSH intervals based on the following criteria:

$$\text{MSH type} = \begin{cases} \tilde{Q}_{\parallel}(\bar{\sigma}_B, A_i), & \text{if } \bar{\sigma}_B > \bar{\sigma}_{B,lim} \;\; \& \;\; A_i < A_{i,lim} \\ \tilde{Q}_{\perp}(\bar{\sigma}_B, A_i), & \text{if } \bar{\sigma}_B < \bar{\sigma}_{B,lim} \;\; \& \;\; A_i > A_{i,lim} \\ \text{undefined}, & \text{otherwise.} \end{cases} \tag{8}$$

In Figure 6b, we show the percentage of undefined intervals for different values of $\bar{\sigma}_{B,lim}$ and $A_{i,lim}$. There are three local minima, two of which correspond to all intervals being categorized as either $\tilde{Q}_{\parallel}$ (top left corner) or $\tilde{Q}_{\perp}$ (bottom right corner). The non-trivial minimum, with a percentage of undefined intervals of 8.6 %, occurs at $\bar{\sigma}_{B,lim} \approx 0.3$ and $A_{i,lim} \approx 0.2$. Values below 9 % are found for $0.25 < \bar{\sigma}_{B,lim} < 0.32$ (vertical lines in Figure 6b) and $0.15 < A_{i,lim} < 0.21$ (horizontal lines). We also show these ranges as shaded regions in Figure 6a to give an indication of the uncertainty in the thresholds. We take the center values, $\bar{\sigma}_{B,lim} = 0.29$ and $A_{i,lim} = 0.18$, as the optimal threshold values in the subsequent analysis.

To find the threshold for $F_{high}$, we first limit the data set to intervals where $E_{i,bulk+th} < 6$ keV. Figure 6c shows histograms of $F_{high}$ separated by the classification from $\bar{\sigma}_{B,lim}$ and $A_{i,lim}$. Overall, the intervals labeled $\tilde{Q}_{\parallel}(\bar{\sigma}_B, A_i)$ (red) have high values of $F_{high}$ and $\tilde{Q}_{\perp}(\bar{\sigma}_B, A_i)$ (blue) have lower $F_{high}$, but the distributions overlap. We then group the intervals based on $\bar{\sigma}_B$, $A_i$, and $F_{high}$:

$$\text{MSH type} = \begin{cases} \tilde{Q}_{\parallel}(\bar{\sigma}_B, A_i, F), & \text{if } \tilde{Q}_{\parallel}(\bar{\sigma}_B, A_i) \;\; \& \;\; F_{high} > F_{high,lim} \\ \tilde{Q}_{\perp}(\bar{\sigma}_B, A_i, F), & \text{if } \tilde{Q}_{\perp}(\bar{\sigma}_B, A_i) \;\; \& \;\; F_{high} < F_{high,lim} \\ \text{undefined}, & \text{otherwise.} \end{cases} \tag{9}$$

We show the percentages of these three categories as a function of $F_{high,lim}$ in Figure 6d. The number of undefined intervals is minimized at $F_{high,lim} = 5 \times 10^5$ keV/(cm$^2$ s sr), and we take this as the optimal threshold to distinguish between the $\tilde{Q}_{\parallel}$ and $\tilde{Q}_{\perp}$ MSH. The minimum value of the percentage of undefined intervals based on $F_{high}$ is 24.7 %, and the percentage stays below 27 % in the range $F_{high,lim} \in (2.8, 6.7) \times 10^5$ keV/(cm$^2$ s sr). We show this range shaded in gray to give an indication of the uncertainty in $F_{high,lim}$.

We summarize the limits in the local parameters in Table 1. These values, found by minimizing the number of undefined intervals, provide a classification of a given interval in the MSH as either $\tilde{Q}_{\parallel}$ or $\tilde{Q}_{\perp}$. In Table S1, we also give the classification of each individual interval based on $\theta_{Bn}$, $(\bar{\sigma}_B, A_i)$, and $F_{high}$.

## 4. Discussion

We analyzed local plasma measurements by MMS in the Earth's MSH and found that they can be used to identify two distinct MSH categories: $\tilde{Q}_{\parallel}$ with stronger magnetic field fluctuations $\bar{\sigma}_{\mathrm{B}}$, low ion temperature anisotropy $A_i$, and high energetic ion flux $F_{\mathrm{high}}$, and $\tilde{Q}_{\perp}$ with lower $\bar{\sigma}_{\mathrm{B}}$, higher $A_i$ and lower $F_{\mathrm{high}}$. The $\tilde{Q}_{\parallel}$ MSH is typically associated with quasi-parallel shocks ($\theta_{\mathrm{Bn}} < 45°$) and $\tilde{Q}_{\perp}$ MSH is more common downstream of quasi-perpendicular shocks ($\theta_{\mathrm{Bn}} > 45°$). MSH intervals in the overlap region $\theta_{\mathrm{Bn}} \in [40°, 70°]$ can present as either $\tilde{Q}_{\parallel}$ or $\tilde{Q}_{\perp}$, which may be attributed to the variation of the ion foreshock boundary. Another possible explanation could be the foreshock properties gradually transitioning from $\tilde{Q}_{\parallel}$ to $\tilde{Q}_{\perp}$; for example, as seen in simulations of the suprathermal ion density (Turc et al., 2018) and magnetic fluctuations (Strumik et al., 2015; Turc et al., 2018, 2022). Since the double-peaked distributions support that two distinct configurations also exist in the overlap region (see Figures 5f–5h, light gray), we favor the moving foreshock boundary as the dominant factor.

Using the normalized magnetic fluctuation level $\bar{\sigma}_{\mathrm{B}}$ and ion temperature anisotropy $A_i$, we can classify 54 % of our data set as $\tilde{Q}_{\parallel}$ and 37 % as $\tilde{Q}_{\perp}$, leaving 9 % undefined. The optimal threshold values in $\bar{\sigma}_{\mathrm{B}}$ and $A_i$ are 0.29 (0.25 − 0.32) and 0.18 (0.15 − 0.21), respectively (parentheses showing ranges with an undefined percentage withing 5 % from the minimum value). When comparing $\bar{\sigma}_{\mathrm{B}}$ and $A_i$ to $\theta_{\mathrm{Bn}}$ calculated from a model (see Figures 4 and 5), we confirm that the overlap region $40° \leq \theta_{\mathrm{Bn}} \leq 70°$ contains both $\tilde{Q}_{\parallel}$ and $\tilde{Q}_{\perp}$ intervals. In this range, the local parameters $\bar{\sigma}_{\mathrm{B}}$ and $A_i$ are still mutually consistent, that is, low $\bar{\sigma}_{\mathrm{B}}$ corresponds to high $A_i$ and vice versa. This motivates a classification of the MSH independently of $\theta_{\mathrm{Bn}}$. We calculate thresholds in the local parameters independently of $\theta_{\mathrm{Bn}}$ because of the different conditions found in the interval $40° \leq \theta_{\mathrm{Bn}} \leq 70°$, and uncertainties in the propagation of L1 measurements to the BS. Karlsson et al. (2021) measure $\boldsymbol{B}_{\mathrm{SW}}$ closer to the BS and use the directly measured $\theta_{\mathrm{Bn}}$ to benchmark the local parameter based classification. They argue that the choice of thresholds depends on the specific application, as there is often a trade-off between minimizing the number of false negatives and the number of false positives. While our approaches differ, our thresholds are within the ranges of the limits suggested by Karlsson et al. (2021). If necessary, one could adjust our thresholds in Table 1 based on our results in Figures 4 and 5 for a more conservative or inclusive classification.

We find that the energetic ion flux, quantified with the parameter $F_{\mathrm{high}}$, exhibits the expected dependence on $\theta_{\mathrm{Bn}}$ overall, with higher values $\left(F_{\mathrm{high}} > 5 \times 10^5 \text{ keV}/\left(\text{cm}^2 \text{ s sr}\right)\right)$ for $\theta_{\mathrm{Bn}} < 70°$ and lower for $\theta_{\mathrm{Bn}} > 40°$. When combining $\bar{\sigma}_{\mathrm{B}}$, $A_i$, and $F_{\mathrm{high}}$, we can classify 55 % of the intervals as $\tilde{Q}_{\parallel}$ and 20 % as $\tilde{Q}_{\perp}$, while 25 % remain undefined. The classification from $F_{\mathrm{high}}$ is mostly consistent with $\bar{\sigma}_{\mathrm{B}}$ and $A_i$, an exception being a CME impact that resulted in a low-$\bar{\sigma}_{\mathrm{B}}$ and high-$A_i$ MSH (corresponding to $\tilde{Q}_{\perp}$) but high-$F_{\mathrm{high}}$ (consistent with $\tilde{Q}_{\parallel}$ MSH), even after removing high-speed and high-temperature intervals. Other structures such as hot flow anomalies can also affect the high-energy ion distributions near the BS (Schwartz et al., 2018), showing that the impact of upstream transients on high-energy MSH ions should be investigated more closely.

A physical limitation to $F_{\mathrm{high}}$ is its relevance only for moderate speed and temperature. Previous studies of ion acceleration at the BS (Johlander et al., 2021; Lalti et al., 2022) used an energy limit of 10 times the solar wind bulk energy. Since the solar wind energy is the upper limit for the thermal energy in the MSH, it makes physical sense to define the suprathermal ion energy relative to it. For $F_{\mathrm{high}}$, we use a constant energy limit of ∼9 keV and find that $F_{\mathrm{high}}$ is a reasonable measure for energetic ions when the bulk speed and temperature are not too high $(E_{i,\mathrm{bulk+th}} < 6 \text{ keV})$. In high-speed/high-temperature cases, $F_{\mathrm{high}}$ includes the thermal ion population and not only the suprathermal part. Unusually high values of $F_{\mathrm{high}}$ have previously been observed in both the $Q_{\parallel}$ and $Q_{\perp}$ MSH in events of high-speed streams in the upstream solar wind plasma (Koller et al., 2024). The higher bulk energy described above could provide an explanation for the high flux of energetic ions. This, however, does not rule out that other processes related to different upstream conditions may affect the ion acceleration at the BS. We recommend exploring new ways of quantifying the presence of energetic ions. A more physically consistent, albeit computationally expensive, method would involve shifting the ion distribution to the ion bulk frame and adjusting the energy limit to the ion temperature. Considering these uncertainties and caveats, $F_{\mathrm{high}}$ remains a blunt measure for classifying the MSH and without knowledge about upstream conditions such as CMEs or high-speed streams, a combination of $\bar{\sigma}_{\mathrm{B}}$ and $A_i$ is more suitable to classify the MSH.



21699402, 2025, 1, Downloaded from https://agupubs.onlinelibrary.wiley.com/doi/10.1029/2024JA033272 by University Of Helsinki, Wiley Online Library on [03/03/2025]. See the Terms and Conditions (https://onlinelibrary.wiley.com/terms-and-conditions) on Wiley Online Library for rules of use; OA articles are governed by the applicable Creative Commons License

21699402, 2025, 1, Downloaded from https://agupubs.onlinelibrary.wiley.com/doi/10.1029/2024JA033272 by University Of Helsinki, Wiley Online Library on [03/03/2025]. See the Terms and Conditions (https://onlinelibrary.wiley.com/terms-and-conditions) on Wiley Online Library for rules of use; OA articles are governed by the applicable Creative Commons License

We observe a weak dependence in $A_i$ (Figure 4c) and $F_{\text{high}}$ (Figure 4d) on the fractional MP/BS distance $d_{\text{MP}-\text{BS}}$. There is a higher observed $A_i$ close to the MP, consistent with previous observations (Dimmock et al., 2015; Soucek et al., 2015). However, the variation did not have a large impact on the classification since the higher $A_i$ increased the difference between the $\tilde{Q}_\perp$ and $\tilde{Q}_\parallel$ MSH. There is also an increased flux of energetic ions close to the MP in the $Q_\perp$ MSH, even after removing intervals with high speed and temperature. High-energy ions may originate from the MP as suggested by for example, Sibeck et al. (1987), but further analysis would be needed to confirm this scenario. In the $Q_\parallel$ MSH, $F_{\text{high}}$ is an order of magnitude lower on the flanks ($|Y_{\text{GSE}}| \gtrsim 20R_{\text{E}}$) than in the subsolar region, which can indicate a decrease in the ion acceleration efficiency (see Figure S1 in Supporting Information S1). Our data set has a limited coverage at the flanks and close to the MP (see Figure S1 in Supporting Information S1). The $Q_\parallel$ intervals only covered $d_{\text{MP}-\text{BS}} \gtrsim 0.5$, and the $Q_\perp$ intervals were collected close to the subsolar region with $|Y_{\text{GSE}}| < 10R_{\text{E}}$ (yellow trajectories in Figure 1). Therefore, we are not able to determine if the same trends with $d_{\text{MP}-\text{BS}}$ and $Y_{\text{GSE}}$ occur in both MSH configurations. For such investigations, more MSH campaigns can help build an even more comprehensive data set.

## 5. Conclusions

We have performed the classification of the Earth's magnetosheath (MSH) using local measurements from the MMS mission. The magnetic fluctuation level $\bar{\sigma}_{\text{B}} = \sigma_{30\text{s}}(\boldsymbol{B})/\langle B \rangle$, ion temperature anisotropy $A_i = T_{i\perp}/T_{i\parallel} - 1$, and the energetic ion flux $F_{\text{high}}$ separate most of the MSH intervals into two distinct configurations which we label $\tilde{Q}_\parallel$ (for $Q_\parallel$-like MSH) and $\tilde{Q}_\perp$ (for $Q_\perp$-like MSH). The $\tilde{Q}_\parallel$ MSH is characterized by high $\bar{\sigma}_{\text{B}}$, low $A_i$, and high $F_{\text{high}}$ while the $\tilde{Q}_\perp$ MSH has low $\bar{\sigma}_{\text{B}}$, high $A_i$, and low $F_{\text{high}}$. We define the $\tilde{Q}_\parallel$ and $\tilde{Q}_\perp$ MSH solely by local measurements, the main physical difference between the two being whether the BS is downstream of the foreshock or not. When comparing to the BS normal angle $\theta_{\text{Bn}}$ calculated from a model, we observed $\tilde{Q}_\parallel$ MSH at $\theta_{\text{Bn}} < 70°$ and $\tilde{Q}_\perp$ MSH at $\theta_{\text{Bn}} > 40°$. In the interval $40° \leq \theta_{\text{Bn}} \leq 70°$ we observed both $\tilde{Q}_\parallel$ and $\tilde{Q}_\perp$ MSH, consistent with the variation of the position of the ion foreshock edge.

The trends in the local parameters with $\theta_{\text{Bn}}$ are consistent with previous results by Karlsson et al. (2021) using Cluster data. In this work, we extended the analysis to a larger data set (27.4 hr) and applied it to MMS data. Our analysis shows that the normalized quantity $\bar{\sigma}_{\text{B}}$ better separates the $\tilde{Q}_\parallel$ from the $\tilde{Q}_\perp$ MSH than $\sigma_{30\text{s}}(\boldsymbol{B})$.

We identified two caveats related to the usage of $F_{\text{high}}$ and we conclude that it should be used with caution. Specific to MMS, compression of fast-mode data overestimates $F_{\text{high}}$, and burst-mode data is therefore necessary to properly detect energetic ions. With data from any spacecraft, $F_{\text{high}}$ increases with high ion speed or temperature due to the constant lower integration limit. For future use, we recommend implementing more detailed methods involving the shifting of the distribution function and taking into account the temperature when quantifying the presence of energetic ions.

We conclude that a combination of $\bar{\sigma}_{\text{B}}$ and $A_i$ provides a good marker of whether the measurement is characteristic of $\tilde{Q}_\parallel$ or $\tilde{Q}_\perp$ MSH. We identified limits at $\bar{\sigma}_{\text{B,lim}} = 0.29$ and $A_{i,\text{lim}} = 0.18$, which left the smallest percentage (8.8 %) of the intervals undefined. The energetic ion flux gives an additional indication using the limit $F_{\text{high,lim}} = 5 \times 10^5$ keV/$\left(\text{cm}^2\ \text{s}\ \text{sr}\right)$, provided that MMS burst-mode data is used. However, some information about upstream conditions such as CME impacts or high-speed streams is required to correctly interpret $F_{\text{high}}$.

Our classification using $\bar{\sigma}_{\text{B}}$ and $A_i$ can be applied to other MMS data sets, for example, to the new unbiased campaign from spring 2024. Also, since $\bar{\sigma}_{\text{B}}$ and $A_i$ are not limited to burst data, the classification can be applicable to longer periods with fast-mode data available. Finally, $\bar{\sigma}_{\text{B}}$ and $A_i$ are independent of instrument noise levels, making our classification applicable for potential future science missions such as Plasma Observatory (Retinò et al., 2022).

## Data Availability Statement

MMS data are available at https://lasp.colorado.edu/mms/sdc/public/data/ following the directories: mms#/fgm/brst/l2 for FGM data, mms#/fpi/brst/l2/dis-dist for FPI ion distributions, and mms#/fpi/brst/l2/dis-moms for FPI

ion moments. Data analysis was performed using the IRFU-Matlab analysis package. No new data has been produced as part of this project.

**Acknowledgments**
We thank the entire MMS team and instrument PIs for data access and support. This work is supported by the Swedish Research Council Grant 2016-0550 and the Swedish National Space Agency Grant 158/16. EY is supported by the Swedish National Space Agency Grant 145/18 and 192/20. GC acknowledges the Academy of Finland Grant 345701. This work is supported by the Knut and Alice Wallenberg foundation (Dnr. 2022.0087).

## References

Alexandrova, O., Lacombe, C., & Mangeney, A. (2008). Spectra and anisotropy of magnetic fluctuations in the Earth's magnetosheath: Cluster observations. *Annales Geophysicae*, *26*(11), 3585–3596. https://doi.org/10.5194/angeo-26-3585-2008

Angelopoulos, V. (2008). The THEMIS Mission. *Space Science Reviews*, *141*(1), 5–34. https://doi.org/10.1007/s11214-008-9336-1

Asbridge, J. R., Bame, S. J., Gosling, J. T., Paschmann, G., & Sckopke, N. (1978). Energetic plasma ions within the Earth's magnetosheath. *Geophysical Research Letters*, *5*(11), 953–955. https://doi.org/10.1029/GL005i011p00953

Barrie, A. C., Smith, D. L., Elkington, S. R., Sternovsky, Z., Silva, D., Giles, B. L., & Schiff, C. (2019). Wavelet compression performance of MMS/FPI plasma count data with plasma environment. *Earth and Space Science*, *6*(1), 116–135. https://doi.org/10.1029/2018EA000430

Barrie, A. C., Smith, S. E., Dorelli, J. C., Gershman, D. J., Yeh, P., Schiff, C., & Avanov, L. A. (2017). Performance of a space-based wavelet compressor for plasma count data on the MMS Fast Plasma Investigation. *Journal of Geophysical Research: Space Physics*, *122*(1), 765–779. https://doi.org/10.1002/2016JA022645

Borovsky, J. E. (2018). The spatial structure of the oncoming solar wind at Earth and the shortcomings of a solar-wind monitor at L1. *Journal of Atmospheric and Solar-Terrestrial Physics*, *177*, 2–11. https://doi.org/10.1016/j.jastp.2017.03.014

Breuillard, H., Matteini, L., Argall, M. R., Sahraoui, F., Andriopoulou, M., Contel, O. L., et al. (2018). New insights into the nature of turbulence in the Earth's magnetosheath using Magnetospheric Multiscale mission data. *The Astrophysical Journal*, *859*(2), 127. https://doi.org/10.3847/1538-4357/aabae8

Burch, J. L., Moore, T. E., Torbert, R. B., & Giles, B. L. (2016). Magnetospheric Multiscale overview and science objectives. *Space Science Reviews*, *199*(1–4), 5–21. https://doi.org/10.1007/s11214-015-0164-9

Burgess, D., Möbius, E., & Scholer, M. (2012). Ion acceleration at the Earth's bow shock. *Space Science Reviews*, *173*(1–4), 5–47. https://doi.org/10.1007/s11214-012-9901-5

Chasapis, A., Matthaeus, W. H., Parashar, T. N., Wan, M., Haggerty, C. C., Pollock, C. J., et al. (2018). In situ observation of intermittent dissipation at kinetic scales in the Earth's magnetosheath. *The Astrophysical Journal Letters*, *856*(1), L19. https://doi.org/10.3847/2041-8213/aaadf8

Chasapis, A., Retinò, A., Sahraoui, F., Vaivads, A., Khotyaintsev, Y. V., Sundkvist, D., et al. (2015). Thin current sheets and associated electron heating in turbulent space plasma. *The Astrophysical Journal*, *804*(1), L1. https://doi.org/10.1088/2041-8205/804/1/L1

Crooker, N. U., Eastman, T. E., Frank, L. A., Smith, E. J., & Russell, C. T. (1981). Energetic magnetosheath ions and the interplanetary magnetic field orientation. *Journal of Geophysical Research*, *86*(A6), 4455–4460. https://doi.org/10.1029/JA086iA06p04455

Czaykowska, A., Bauer, T. M., Treumann, R. A., & Baumjohann, W. (2001). Magnetic field fluctuations across the Earth's bow shock. *Annales Geophysicae*, *19*(3), 275–287. https://doi.org/10.5194/angeo-19-275-2001

Di Matteo, S., & Sivadas, N. (2022). Solar-wind/magnetosphere coupling: Understand uncertainties in upstream conditions. *Frontiers in Astronomy and Space Sciences*, *9*, 1060072. https://doi.org/10.3389/fspas.2022.1060072

Dimmock, A. P., & Nykyri, K. (2013). The statistical mapping of magnetosheath plasma properties based on THEMIS measurements in the magnetosheath interplanetary medium reference frame. *Journal of Geophysical Research: Space Physics*, *118*(8), 4963–4976. https://doi.org/10.1002/jgra.50465

Dimmock, A. P., Nykyri, K., Osmane, A., Karimabadi, H., & Pulkkinen, T. I. (2017). Dawn-dusk asymmetries of the Earth's dayside magnetosheath in the magnetosheath interplanetary medium reference frame. In S. Haaland, A. Runov, & C. Forsyth (Eds.), *Geophysical Monograph Series* (1st ed., pp. 49–72). Wiley. https://doi.org/10.1002/9781119216346.ch5

Dimmock, A. P., Nykyri, K., & Pulkkinen, T. I. (2014). A statistical study of magnetic field fluctuations in the dayside magnetosheath and their dependence on upstream solar wind conditions. *Journal of Geophysical Research: Space Physics*, *119*(8), 6231–6248. https://doi.org/10.1002/2014JA020009

Dimmock, A. P., Osmane, A., Pulkkinen, T. I., & Nykyri, K. (2015). A statistical study of the dawn-dusk asymmetry of ion temperature anisotropy and mirror mode occurrence in the terrestrial dayside magnetosheath using THEMIS data. *Journal of Geophysical Research: Space Physics*, *120*(7), 5489–5503. https://doi.org/10.1002/2015JA021192

Dunlop, M. W., Dong, X., Wang, T., Eastwood, J. P., Robert, P., Haaland, S., et al. (2021). Curlometer technique and applications. *Journal of Geophysical Research: Space Physics*, *126*(11), e2021JA029538. https://doi.org/10.1029/2021JA029538

Eriksson, E., Vaivads, A., Graham, D. B., Khotyaintsev, Y. V., Yordanova, E., Hietala, H., et al. (2016). Strong current sheet at a magnetosheath jet: Kinetic structure and electron acceleration. *Journal of Geophysical Research: Space Physics*, *121*(10), 9608–9618. https://doi.org/10.1002/2016JA023146

Eriksson, S., Wilder, F., Ergun, R., Schwartz, S., Cassak, P., Burch, J., et al. (2016). Magnetospheric Multiscale observations of the electron diffusion region of large guide field magnetic reconnection. *Physical Review Letters*, *117*(1), 015001. https://doi.org/10.1103/PhysRevLett.117.015001

Escoubet, C. P., Schmidt, R., & Goldstein, M. L. (1997). Cluster - Science and Mission Overview. In C. P. Escoubet, C. T. Russell, & R. Schmidt (Eds.), *The Cluster and Phoenix Missions* (pp. 11–32). Springer Netherlands. https://doi.org/10.1007/978-94-011-5666-0_1

Fairfield, D. H., Iver, H. C., Desch, M. D., Szabo, A., Lazarus, A. J., & Aellig, M. R. (2001). The location of low Mach number bow shocks at Earth. *Journal of Geophysical Research*, *106*(A11), 25361–25376. https://doi.org/10.1029/2000JA000252

Farris, M. H., Petrinec, S. M., & Russell, C. T. (1991). The thickness of the magnetosheath: Constraints on the polytropic index. *Geophysical Research Letters*, *18*(10), 1821–1824. https://doi.org/10.1029/91GL02090

Farris, M. H., & Russell, C. T. (1994). Determining the standoff distance of the bow shock: Mach number dependence and use of models. *Journal of Geophysical Research*, *99*(A9), 17681–17689. https://doi.org/10.1029/94JA01020

Fuselier, S. A., Klumpar, D. M., & Shelley, E. G. (1991). On the origins of energetic ions in the Earth's dayside magnetosheath. *Journal of Geophysical Research*, *96*(A1), 47–56. https://doi.org/10.1029/90JA01751

Fuselier, S. A., Lewis, W. S., Schiff, C., Ergun, R., Burch, J. L., Petrinec, S. M., & Trattner, K. J. (2016). Magnetospheric Multiscale science mission profile and operations. *Space Science Reviews*, *199*(1–4), 77–103. https://doi.org/10.1007/s11214-014-0087-x

Génot, V., Broussillou, L., Budnik, E., Hellinger, P., Trávníček, P. M., Lucek, E., & Dandouras, I. (2011). Timing mirror structures observed by Cluster with a magnetosheath flow model. *Annales Geophysicae*, *29*(10), 1849–1860. https://doi.org/10.5194/angeo-29-1849-2011

Gutynska, O., Šafránková, J., & Němeček, Z. (2008). Correlation length of magnetosheath fluctuations: Cluster statistics. *Annales Geophysicae*, *26*(9), 2503–2513. https://doi.org/10.5194/angeo-26-2503-2008



21699402, 2025, 1, Downloaded from https://agupubs.onlinelibrary.wiley.com/doi/10.1029/2024JA033272 by University Of Helsinki, Wiley Online Library on [03/03/2025]. See the Terms and Conditions (https://onlinelibrary.wiley.com/terms-and-conditions) on Wiley Online Library for rules of use; OA articles are governed by the applicable Creative Commons License

Hietala, H., Laitinen, T. V., Andréeová, K., Vainio, R., Vaivads, A., Palmroth, M., et al. (2009). Supermagnetosonic jets behind a collisionless quasiparallel shock. *Physical Review Letters*, *103*(24), 245001. https://doi.org/10.1103/PhysRevLett.103.245001

Jarvinen, R., Vainio, R., Palmroth, M., Juusola, L., Hoilijoki, S., Pfau-Kempf, Y., et al. (2018). Ion acceleration by flux transfer events in the terrestrial magnetosheath. *Geophysical Research Letters*, *45*(4), 1723–1731. https://doi.org/10.1002/2017GL076192

Johlander, A., Battarbee, M., Vaivads, A., Turc, L., Pfau-Kempf, Y., Ganse, U., et al. (2021). Ion acceleration efficiency at the Earth's bow shock: Observations and simulation results. *The Astrophysical Journal*, *914*(2), 82. https://doi.org/10.3847/1538-4357/abfafc

Karlsson, T., Raptis, S., Trollvik, H., & Nilsson, H. (2021). Classifying the magnetosheath behind the quasi-parallel and quasi-perpendicular bow shock by local measurements. *Journal of Geophysical Research: Space Physics*, *126*(9), e2021JA029269. https://doi.org/10.1029/2021JA029269

Kempf, Y., Pokhotelov, D., Gutynska, O., Wilson Iii, L. B., Walsh, B. M., Alfthan, S. V., et al. (2015). Ion distributions in the Earth's foreshock: Hybrid-Vlasov simulation and THEMIS observations. *Journal of Geophysical Research: Space Physics*, *120*(5), 3684–3701. https://doi.org/10.1002/2014JA020519

Koller, F., Raptis, S., Temmer, M., & Karlsson, T. (2024). The effect of fast solar wind on ion distribution downstream of Earth's bow shock. *The Astrophysical Journal Letters*, *964*(1), L5. https://doi.org/10.3847/2041-8213/ad2ddf

Lalti, A., Khotyaintsev, Y. V., Dimmock, A. P., Johlander, A., Graham, D. B., & Olshevsky, V. (2022). A database of MMS bow shock crossings compiled using machine learning. *Journal of Geophysical Research: Space Physics*, *127*(8), e2022JA030454. https://doi.org/10.1029/2022JA030454

Le, G., & Russell, C. (1992). A study of ULF wave foreshock morphology—I: ULF foreshock boundary. *Planetary and Space Science*, *40*(9), 1203–1213. https://doi.org/10.1016/0032-0633(92)90077-2

Luhmann, J. G., Russell, C. T., & Elphic, R. C. (1986). Spatial distributions of magnetic field fluctuations in the dayside magnetosheath. *Journal of Geophysical Research*, *91*(A2), 1711–1715. https://doi.org/10.1029/JA091iA02p01711

Ma, D., An, X., Artemyev, A., Bortnik, J., Angelopoulos, V., & Zhang, X.-J. (2024). Nonlinear Landau resonant interaction between whistler waves and electrons: Excitation of electron-acoustic waves. *Physics of Plasmas*, *31*(2), 022304. https://doi.org/10.1063/5.0171227

Merka, J., Szabo, A., Narock, T. W., King, J. H., Paularena, K. I., & Richardson, J. D. (2003). A comparison of IMP 8 observed bow shock positions with model predictions. *Journal of Geophysical Research*, *108*(A2), 1077. https://doi.org/10.1029/2002JA009384

Michotte De Welle, B., Aunai, N., Lavraud, B., Génot, V., Jeandet, A., Nguyen, G., et al. (2024). Spatial distribution of plasma density and magnetic field amplitude in the dayside magnetosheath as a function of the IMF orientation. *Frontiers in Astronomy and Space Sciences*, *11*, 1427791. https://doi.org/10.3389/fspas.2024.1427791

Narita, Y., Glassmeier, K., Fornaçon, K., Richter, I., Schäfer, S., Motschmann, U., et al. (2006). Low-frequency wave characteristics in the upstream and downstream regime of the terrestrial bow shock. *Journal of Geophysical Research*, *111*(A1), 2005JA011231. https://doi.org/10.1029/2005JA011231

Narita, Y., Plaschke, F., & Vörös, Z. (2021). The magnetosheath. In *Magnetospheres in the solar system* (pp. 137–152). American Geophysical Union (AGU). https://doi.org/10.1002/9781119815624.ch9

Papitashvili, N. E., & King, J. H. (2020). Omni hourly data. *NASA Space Physics Data Facility*. https://doi.org/10.48322/1shr-ht18

Paschmann, G., Sckopke, N., Papamastorakis, I., Asbridge, J. R., Bame, S. J., & Gosling, J. T. (1981). Characteristics of reflected and diffuse ions upstream from the Earth's bow shock. *Journal of Geophysical Research*, *86*(A6), 4355–4364. https://doi.org/10.1029/JA086iA06p04355

Phan, T. D., Eastwood, J. P., Shay, M. A., Drake, J. F., Sonnerup, B. U., Fujimoto, M., et al. (2018). Electron magnetic reconnection without ion coupling in Earth's turbulent magnetosheath. *Nature*, *557*(7704), 202–206. https://doi.org/10.1038/s41586-018-0091-5

Plaschke, F., Hietala, H., & Angelopoulos, V. (2013). Anti-sunward high-speed jets in the subsolar magnetosheath. *Annales Geophysicae*, *31*(10), 1877–1889. https://doi.org/10.5194/angeo-31-1877-2013

Pollock, C., Moore, T., Jacques, A., Burch, J., Gliese, U., Saito, Y., et al. (2016). Fast plasma investigation for Magnetospheric Multiscale. *Space Science Reviews*, *199*(1–4), 331–406. https://doi.org/10.1007/s11214-016-0245-4

Rakhmanova, L., Riazantseva, M., Zastenker, G., & Verigin, M. (2018). Kinetic-scale ion flux fluctuations behind the quasi-parallel and quasi-perpendicular bow shock. *Journal of Geophysical Research: Space Physics*, *123*(7), 5300–5314. https://doi.org/10.1029/2018JA025179

Raptis, S., Karlsson, T., Plaschke, F., Kullen, A., & Lindqvist, P. (2020). Classifying magnetosheath jets using MMS: Statistical properties. *Journal of Geophysical Research: Space Physics*, *125*(11), e2019JA027754. https://doi.org/10.1029/2019JA027754

Retinò, A., Khotyaintsev, Y., Le Contel, O., Marcucci, M. F., Plaschke, F., Vaivads, A., et al. (2022). Particle energization in space plasmas: Towards a multi-point, multi-scale plasma observatory. *Experimental Astronomy*, *54*(2–3), 427–471. https://doi.org/10.1007/s10686-021-09797-7

Retinò, A., Sundkvist, D., Vaivads, A., Mozer, F., André, M., & Owen, C. J. (2007). In situ evidence of magnetic reconnection in turbulent plasma. *Nature Physics*, *3*(4), 235–238. https://doi.org/10.1038/nphys574

Roberts, O. W., Vörös, Z., Torkar, K., Stawarz, J., Bandyopadhyay, R., Gershman, D. J., et al. (2023). Estimation of the error in the calculation of the pressure-strain term: Application in the terrestrial magnetosphere. *Journal of Geophysical Research: Space Physics*, *128*(8), e2023JA031565. https://doi.org/10.1029/2023JA031565

Russell, C. T., Anderson, B. J., Baumjohann, W., Bromund, K. R., Dearborn, D., Fischer, D., et al. (2016). The Magnetospheric Multiscale magnetometers. *Space Science Reviews*, *199*(1–4), 189–256. https://doi.org/10.1007/s11214-014-0057-3

Schwartz, S. J., Avanov, L., Turner, D., Zhang, H., Gingell, I., Eastwood, J. P., et al. (2018). Ion kinetics in a hot flow anomaly: MMS observations. *Geophysical Research Letters*, *45*(21), 11520–11529. https://doi.org/10.1029/2018GL080189

Shevyrev, N., Zastenker, G., & Du, J. (2007). Statistics of low-frequency variations in solar wind, foreshock and magnetosheath: INTERBALL-1 and CLUSTER data. *Planetary and Space Science*, *55*(15), 2330–2335. https://doi.org/10.1016/j.pss.2007.05.014

Shue, J.-H., Song, P., Russell, C. T., Steinberg, J. T., Chao, J. K., Zastenker, G., et al. (1998). Magnetopause location under extreme solar wind conditions. *Journal of Geophysical Research*, *103*(A8), 17691–17700. https://doi.org/10.1029/98JA01103

Sibeck, D. G., McEntire, R. W., Lui, A. T. Y., Krimigis, S. M., Zanetti, L. J., & Potemra, T. A. (1987). The magnetosphere as a source of energetic magnetosheath ions. *Geophysical Research Letters*, *14*(10), 1011–1014. https://doi.org/10.1029/GL014i010p01011

Soucek, J., & Escoubet, C. P. (2012). Predictive model of magnetosheath plasma flow and its validation against Cluster and THEMIS data. *Annales Geophysicae*, *30*(6), 973–982. https://doi.org/10.5194/angeo-30-973-2012

Soucek, J., Escoubet, C. P., & Grison, B. (2015). Magnetosheath plasma stability and ULF wave occurrence as a function of location in the magnetosheath and upstream bow shock parameters. *Journal of Geophysical Research: Space Physics*, *120*(4), 2838–2850. https://doi.org/10.1002/2015JA021087

Stawarz, J. E., Eastwood, J. P., Phan, T. D., Gingell, I. L., Shay, M. A., Burch, J. L., et al. (2019). Properties of the turbulence associated with electron-only magnetic reconnection in Earth's magnetosheath. *The Astrophysical Journal Letters*, *877*(2), L37. https://doi.org/10.3847/2041-8213/ab21c8



21699402, 2025, 1, Downloaded from https://agupubs.onlinelibrary.wiley.com/doi/10.1029/2024JA033272 by University Of Helsinki, Wiley Online Library on [03/03/2025]. See the Terms and Conditions (https://onlinelibrary.wiley.com/terms-and-conditions) on Wiley Online Library for rules of use; OA articles are governed by the applicable Creative Commons License

Strumik, M., Roytershteyn, V., Karimabadi, H., Stasiewicz, K., Grzesiak, M., & Przepiórka, D. (2015). Identification of the dominant ULF wave mode and generation mechanism for obliquely propagating waves in the Earth's foreshock. *Geophysical Research Letters*, *42*(13), 5109–5116. https://doi.org/10.1002/2015GL064915

Svenningsson, I., Yordanova, E., Khotyaintsev, Y. V., André, M., Cozzani, G., & Steinvall, K. (2024). Whistler waves in the quasi-parallel and quasi-perpendicular magnetosheath. *Journal of Geophysical Research: Space Physics*, *129*(6), e2024JA032661. https://doi.org/10.1029/2024JA032661

Treumann, R. A. (2009). Fundamentals of collisionless shocks for astrophysical application, 1. Non-relativistic shocks. *Astronomy and Astrophysics Review*, *17*(4), 409–535. https://doi.org/10.1007/s00159-009-0024-2

Turc, L., Fontaine, D., Savoini, P., & Kilpua, E. K. J. (2014). A model of the magnetosheath magnetic field during magnetic clouds. *Annales Geophysicae*, *32*(2), 157–173. https://doi.org/10.5194/angeo-32-157-2014

Turc, L., Ganse, U., Pfau-Kempf, Y., Hoilijoki, S., Battarbee, M., Juusola, L., et al. (2018). Foreshock properties at typical and enhanced interplanetary magnetic field strengths: Results from Hybrid-Vlasov simulations. *Journal of Geophysical Research: Space Physics*, *123*(7), 5476–5493. https://doi.org/10.1029/2018JA025466

Turc, L., Roberts, O. W., Verscharen, D., Dimmock, A. P., Kajdič, P., Palmroth, M., et al. (2023). Transmission of foreshock waves through Earth's bow shock. *Nature Physics*, *19*(1), 78–86. https://doi.org/10.1038/s41567-022-01837-z

Turc, L., Zhou, H., Tarvus, V., Ala-Lahti, M., Battarbee, M., Pfau-Kempf, Y., et al. (2022). A global view of Pc3 wave activity in near-Earth space: Results from hybrid-Vlasov simulations. *Frontiers in Astronomy and Space Sciences*, *9*, 989369. https://doi.org/10.3389/fspas.2022.989369

Vörös, Z., Yordanova, E., Echim, M. M., Consolini, G., & Narita, Y. (2016). Turbulence-generated proton-scale structures in the terrestrial magnetosheath. *The Astrophysical Journal*, *819*(1), L15. https://doi.org/10.3847/2041-8205/819/1/L15

Vörös, Z., Yordanova, E., Varsani, A., Genestreti, K. J., Khotyaintsev, Y. V., Li, W., et al. (2017). MMS observation of magnetic reconnection in the turbulent magnetosheath. *Journal of Geophysical Research: Space Physics*, *122*(11). https://doi.org/10.1002/2017JA024535

Yordanova, E., Vörös, Z., Raptis, S., & Karlsson, T. (2020). Current sheet statistics in the magnetosheath. *Frontiers in Astronomy and Space Sciences*, *7*, 2. https://doi.org/10.3389/fspas.2020.00002

Yordanova, E., Vörös, Z., Sorriso-Valvo, L., Dimmock, A. P., & Kilpua, E. (2021). A possible link between turbulence and plasma heating. *The Astrophysical Journal*, *921*(1), 65. https://doi.org/10.3847/1538-4357/ac1942

Yordanova, E., Vörös, Z., Varsani, A., Graham, D. B., Norgren, C., Khotyaintsev, Y. V., et al. (2016). Electron scale structures and magnetic reconnection signatures in the turbulent magnetosheath. *Geophysical Research Letters*, *43*(12), 5969–5978. https://doi.org/10.1002/2016GL069191



21699402, 2025, 1, Downloaded from https://agupubs.onlinelibrary.wiley.com/doi/10.1029/2024JA033272 by University Of Helsinki, Wiley Online Library on [03/03/2025]. See the Terms and Conditions (https://onlinelibrary.wiley.com/terms-and-conditions) on Wiley Online Library for rules of use; OA articles are governed by the applicable Creative Commons License